

Radboud Universiteit



Electronic structure and properties of a few-layer black phosphorus

Mikhail Katsnelson

Main collaborators:

Sasha
Rudenko

Shengjun
Yuan

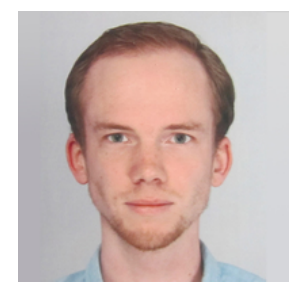
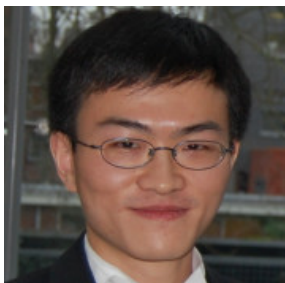
Rafa
Roldan

Sergey
Brener

Clément
Dutreix

Zhenya
Stepanov

Edo
van Veen



Zoo of 2D materials

Plenty of 2D materials starting from graphene

Graphene

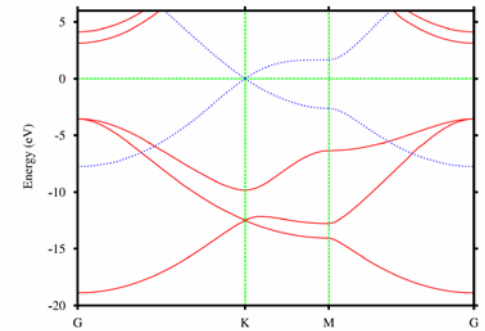
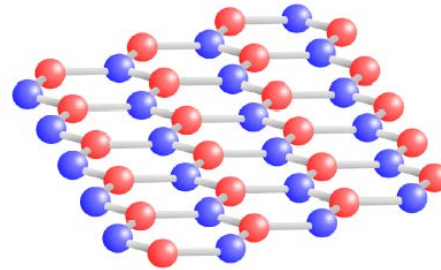
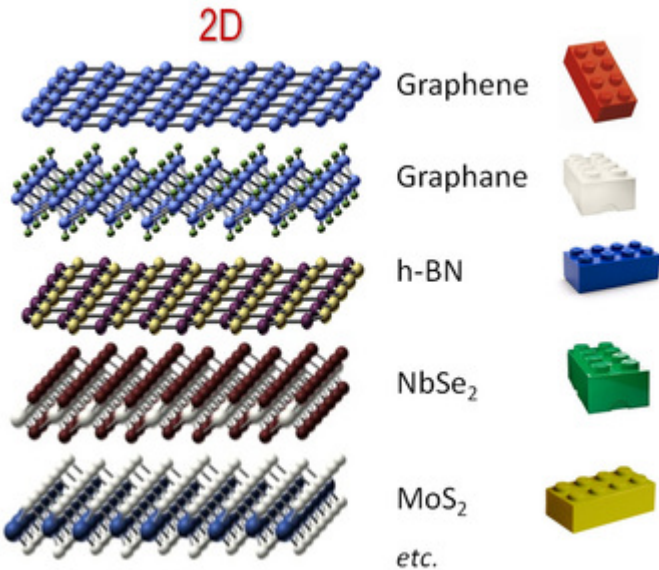
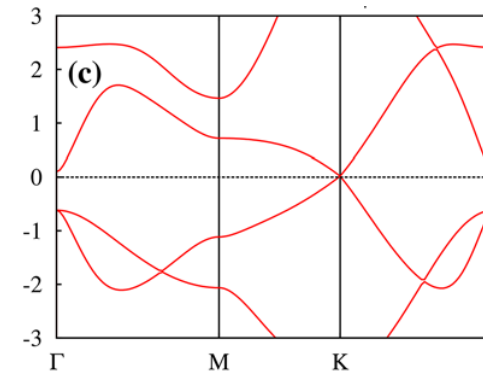
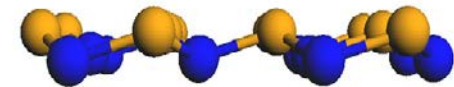
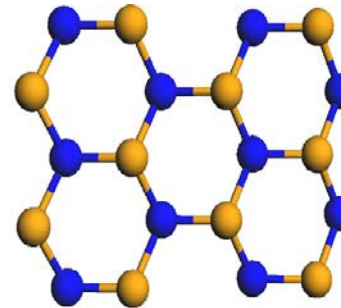


FIG. 2: (color online) Band structure of a single graphene layer. Solid red lines are σ bands and dotted blue lines are π bands.

Silicene, germanene

Buckling



Semimetals (graphene), semiconductors, metals, superconductors, broad-gap insulators...

OPEN ACCESS
IOP Publishing

J. Phys.: Condens. Matter 27 (2015) 443002 (11pp)

Journal of Physics: Condensed Matter

doi:10.1088/0953-8964/27/44/443002

Topical Review

Germanene: the germanium analogue of graphene

A Acun^{1,6}, L Zhang^{1,6}, P Bampoulis¹, M Farmanbar², A van Houselt¹,
A N Rudenko³, M Lingenfelder^{4,5}, G Brocks², B Poelsema¹, M I Katsnelson³
and H J W Zandvliet¹

Zoo of 2D materials II

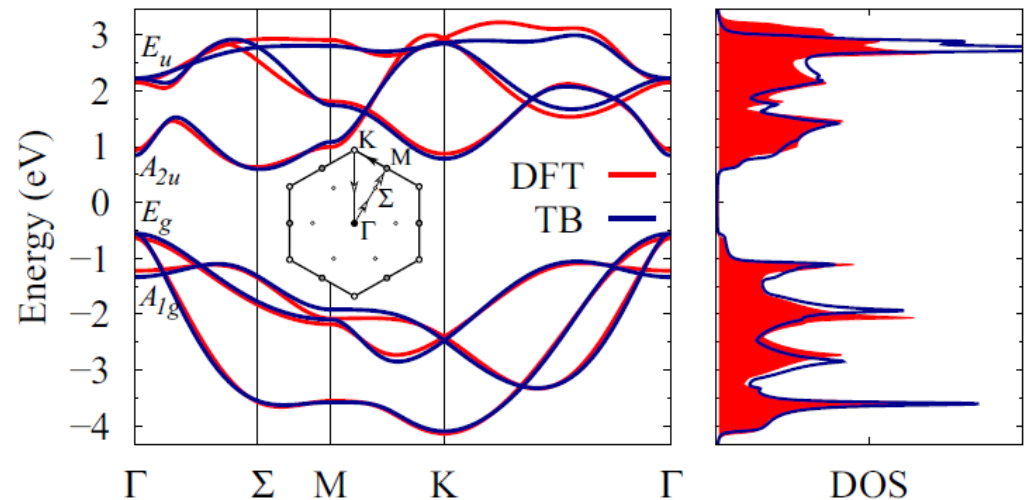
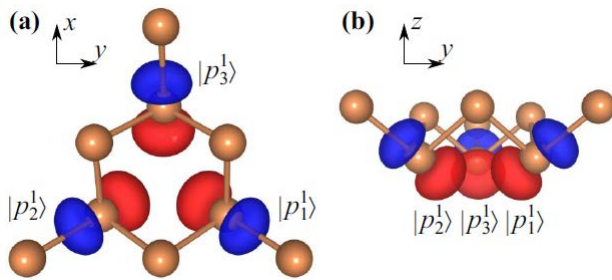
PHYSICAL REVIEW B **95**, 081407(R) (2017)

Antimony

Electronic properties of single-layer antimony: Tight-binding model, spin-orbit coupling, and the strength of effective Coulomb interactions

A. N. Rudenko,^{1,*} M. I. Katsnelson,¹ and R. Roldán²

The same buckled structure as for silicene or germanene



Semiconductor. Strong spin-orbit coupling

$$\lambda = 0.34 \text{ eV}$$

Method	$E_g^{\Gamma\Sigma}$		Holes		Electrons			
	$E_g^{\Gamma\Sigma}$	$E_g^{\Gamma\Gamma}$	m_{Γ}^1	m_{Γ}^2	m_{Γ}	m_{Σ}^x	m_{Σ}^y	m_K
DFT	1.26	1.57	0.08	0.45	0.09	0.14	0.45	0.39
TB	1.15	1.40	0.06	0.44	0.06	0.13	0.42	0.36
DFT+SO	0.99	1.25	0.10	0.19	0.08	0.14	0.46	0.40
TB+SO	0.92	1.14	0.09	0.11	0.06	0.13	0.43	0.37

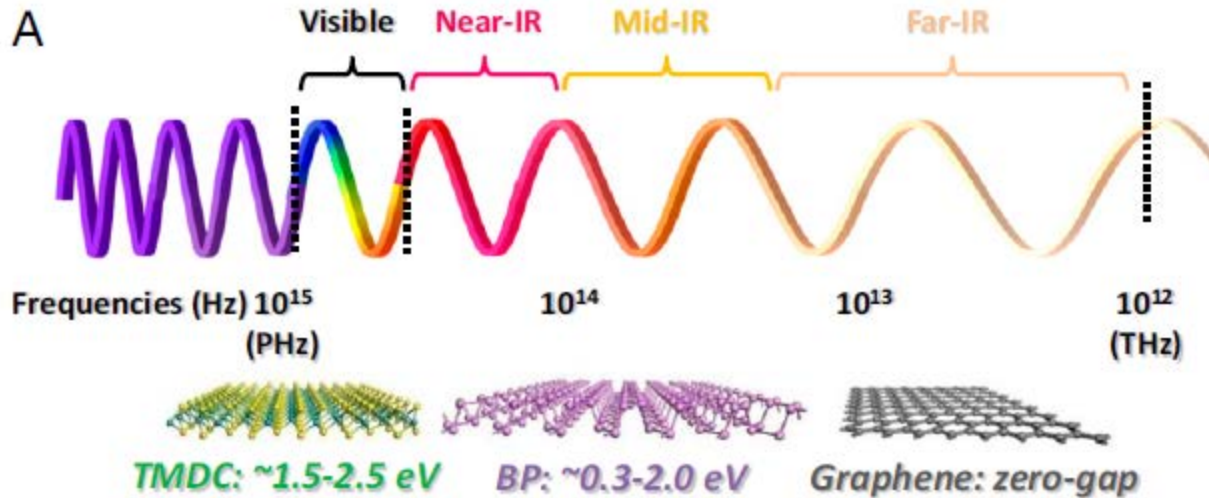
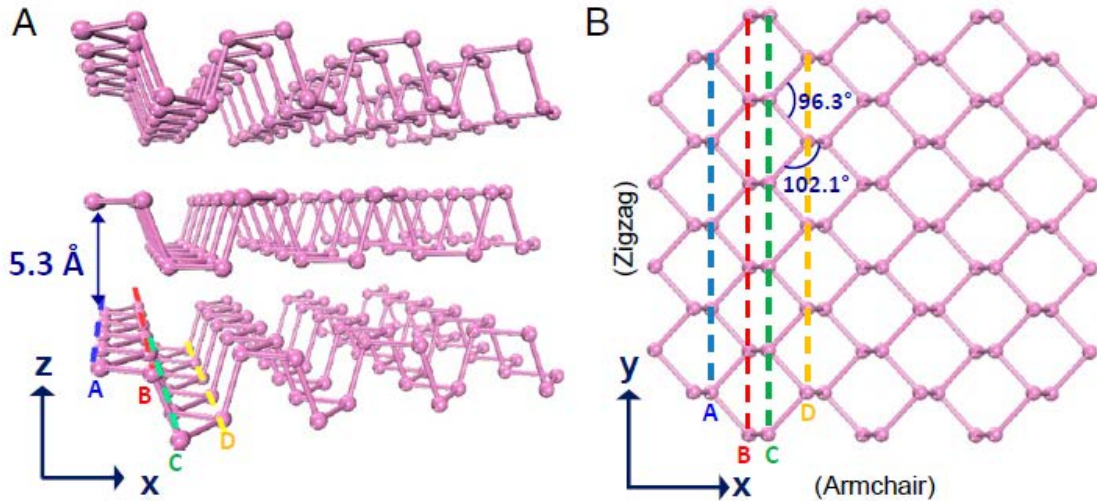
What is BP?

For historical and basic review: Ling et al, PNAS 112, 4523 (2015)

Bridgman (1914)

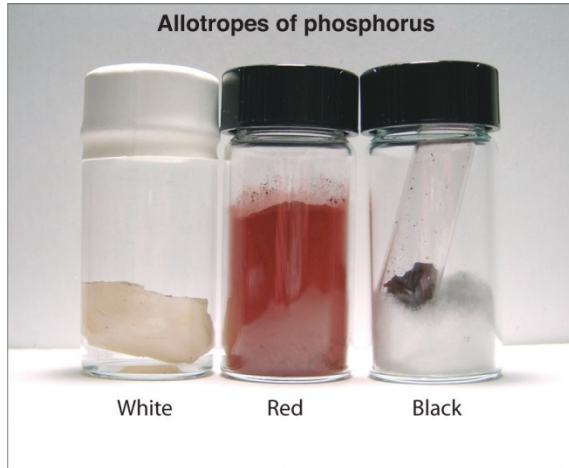
Black P – stable allotrope of P at ambient conditions

Layered compound, 4 atoms per unit cell, bond lengths within layer 0.222 and 0.224 nm, between layers 0.53 nm



Tunable gap, depending on number of layers

Other allopropes of phosphorus



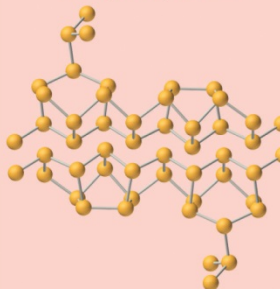
White phosphorus



Volatile waxy white solid. Dangerously reactive in air: glows with a white light and spontaneously bursts into flame. Melting point: 44.2°C

The image shows a ball-and-stick model of a white phosphorus molecule, which is a tetrahedron of four phosphorus atoms (represented by orange spheres).

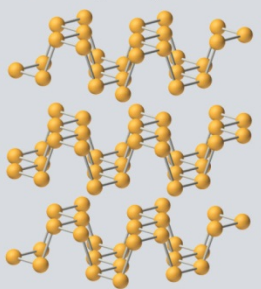
Red phosphorus



Red powder. Nonreactive with air at 25°C. Melting point: 590°C

The image shows a ball-and-stick model of a red phosphorus structure, which is a complex, interconnected network of phosphorus atoms (represented by orange spheres).

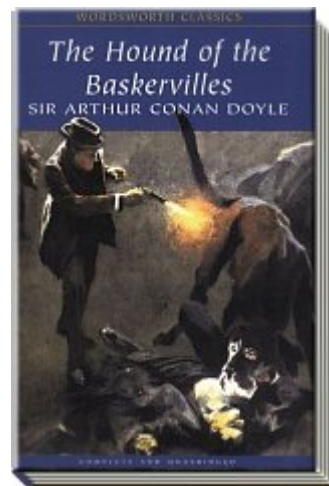
Black phosphorus



Black crystalline solid. Nonreactive with air at 25°C. Melting point: 610°C

The image shows a ball-and-stick model of a black phosphorus structure, which is a layered, crystalline structure of phosphorus atoms (represented by orange spheres).

White phosphorus is most know to a general public (e.g., “phosphorescence”)



Computations of electronic structure

RAPID COMMUNICATIONS

PHYSICAL REVIEW B 89, 201408(R) (2014)

Quasiparticle band structure and tight-binding model for single- and bilayer black phosphorus

A. N. Rudenko* and M. I. Katsnelson

PHYSICAL REVIEW B 92, 085419 (2015)

Toward a realistic description of multilayer black phosphorus: From *GW* approximation to large-scale tight-binding simulations

A. N. Rudenko,* Shengjun Yuan, and M. I. Katsnelson

Gap problem: conventional density functional (LDA or GGA) usually strongly underestimates gaps in semiconductors – more advanced methods should be used like **GW**

Quasiparticle equation:

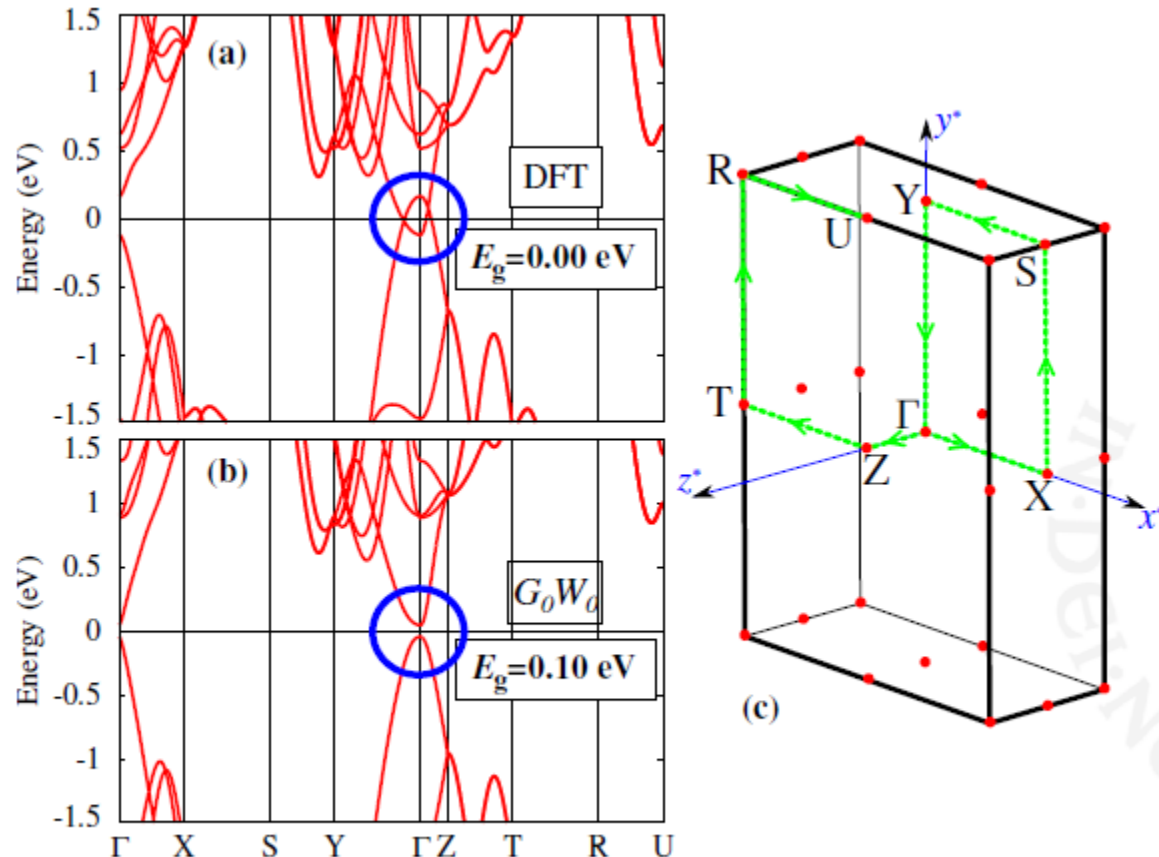
$$(T + V_{n-e} + V_H) + \underbrace{\int \Sigma(\mathbf{r}, \mathbf{r}', E_{nk}) \psi_{nk}(\mathbf{r}') d\mathbf{r}'}_{\text{Self-energy}} = \underbrace{E_{nk}}_{\text{QP energy}} \psi_{nk}(\mathbf{r})$$

Self-energy in the *GW* approximation:

$$\Sigma^{GW}(\mathbf{r}, \mathbf{r}'; \omega) = \frac{i\hbar}{2\pi} \int_{-\infty}^{\infty} \underbrace{G(\mathbf{r}, \mathbf{r}'; \omega + \omega')}_{\text{Green's function}} \underbrace{W(\mathbf{r}, \mathbf{r}'; \omega')}_{\text{Screened Coul. int.}} e^{i\omega'\eta} d\omega'$$

Computations of electronic structure II

Bulk BP



GW fixes the band gap problem

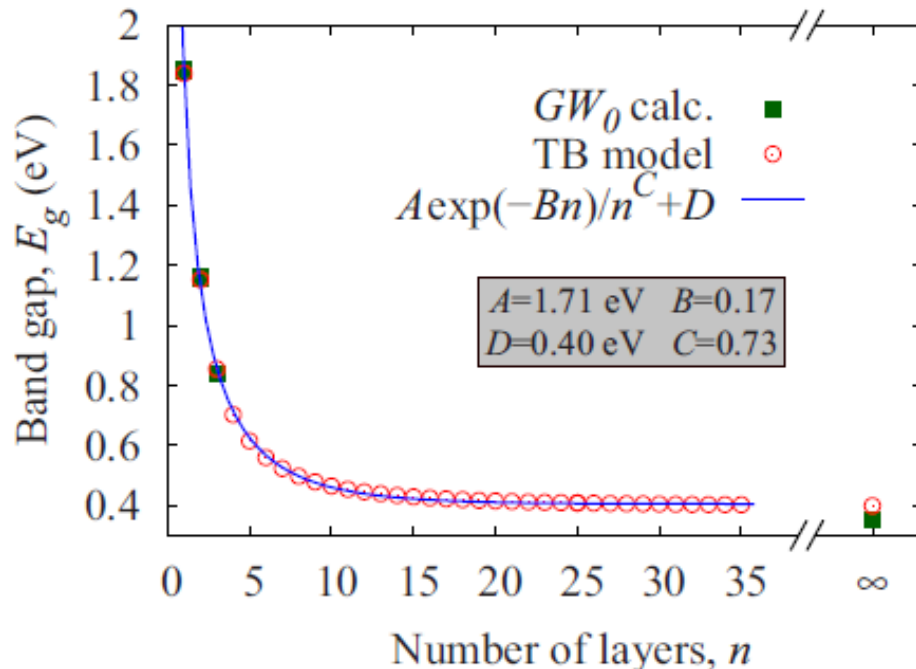
And self-consistency makes the gap accurate, 0.35 eV!

Computations of electronic structure III

TABLE I. Band gaps (in eV) for monolayer ($n = 1$), multilayer ($n = 2,3$), and bulk BP ($n = \infty$) calculated at different levels of theory. In the notation of different methods, G_0 and W_0 imply that the Green's function and screened Coulomb repulsion in the GW approach are calculated non-self-consistently on the basis of wave functions derived from density functional (GGA) or hybrid functional (HSE) calculations, whereas G means a self-consistent calculation of the Green's function. W'_0 and W_0 denote that the screened Coulomb interaction is calculated by using the general plasmon pole model [39] and RPA [40], respectively.

	$GW_0@GGA^a$	TB Model ^a	$GW_0@GGA^b$	$GW_0@HSE^c$	$G_0W_0@GGA^d$	$G_0W'_0@GGA^e$	HSE ^f	GGA ^g	Expt.
$n = 1$	1.85	1.84	1.94	2.41	1.60	2.00	1.00–1.91	0.80–0.91	2.05 ^h
$n = 2$	1.16	1.15	~1.65	1.66	1.01	~1.30	1.01–1.23	0.45–0.60	—
$n = 3$	0.84	0.85	~1.35	1.20	0.68	~1.05	0.73–0.98	0.20–0.40	—
$n = \infty$	0.35	0.40	0.43	0.58	0.10	0.30	0.18–0.39	0.00–0.15	0.31–0.35 ⁱ

^aThis work.



A very strong dependence of the gap on number of layers!

Computations of electronic structure IV

Cohesive energy: QMC calculations

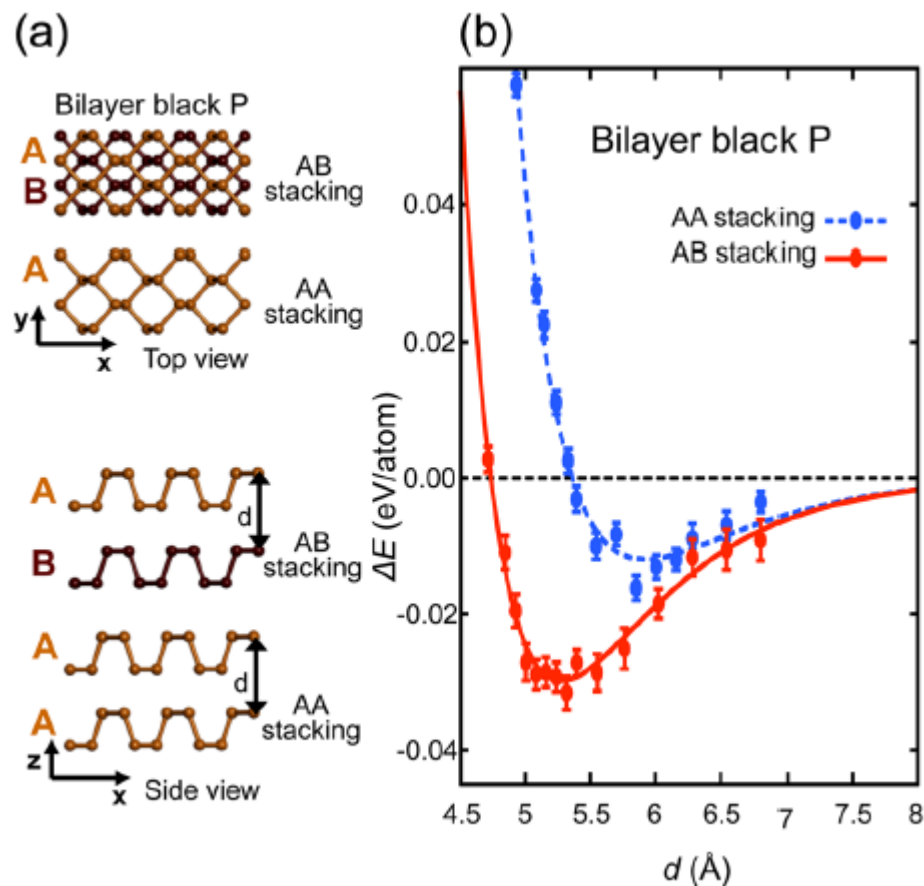
DOI: 10.1021/acs.nanolett.5b03615
Nano Lett. 2015, 15, 8170–8175

The Nature of the Interlayer Interaction in Bulk and Few-Layer Phosphorus

L. Shulenburger,[†] A.D. Baczewski,[†] Z. Zhu,[‡] J. Guan,[‡] and D. Tománek^{*,‡}

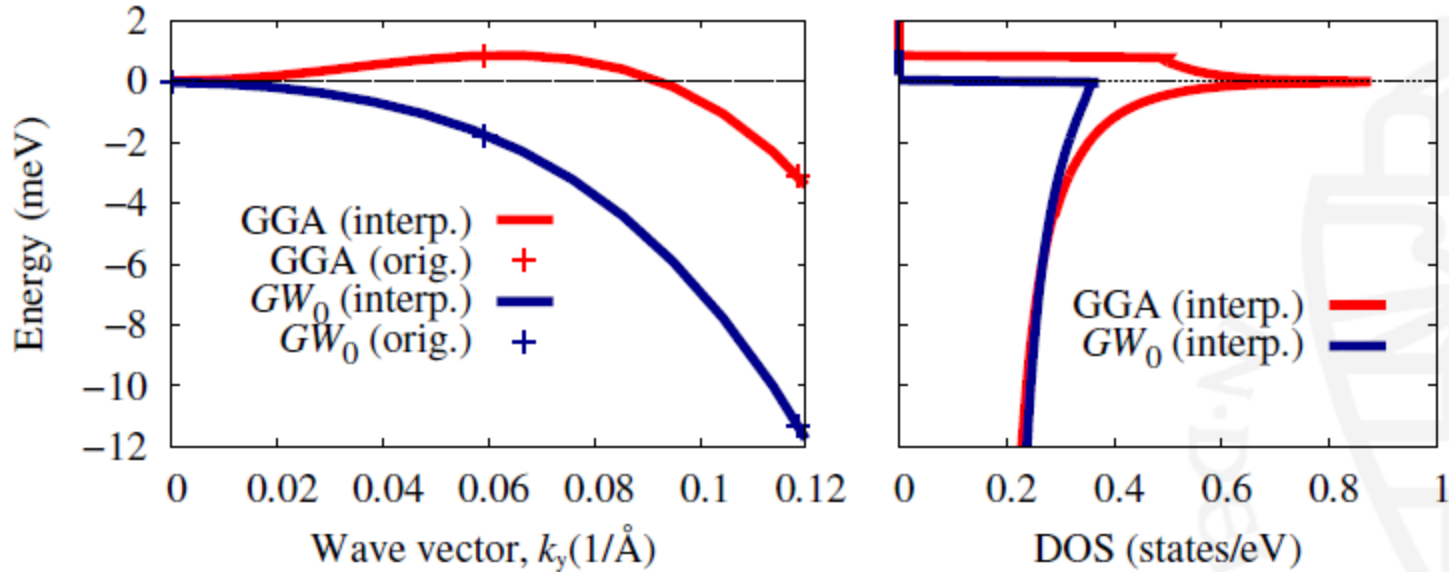
VdW interactions: weak and can hardly be described by conventional density functional

How can it be? How weak cohesive energy is consistent with a huge dependence of interlayer hopping to the gap?!



Computations of electronic structure V

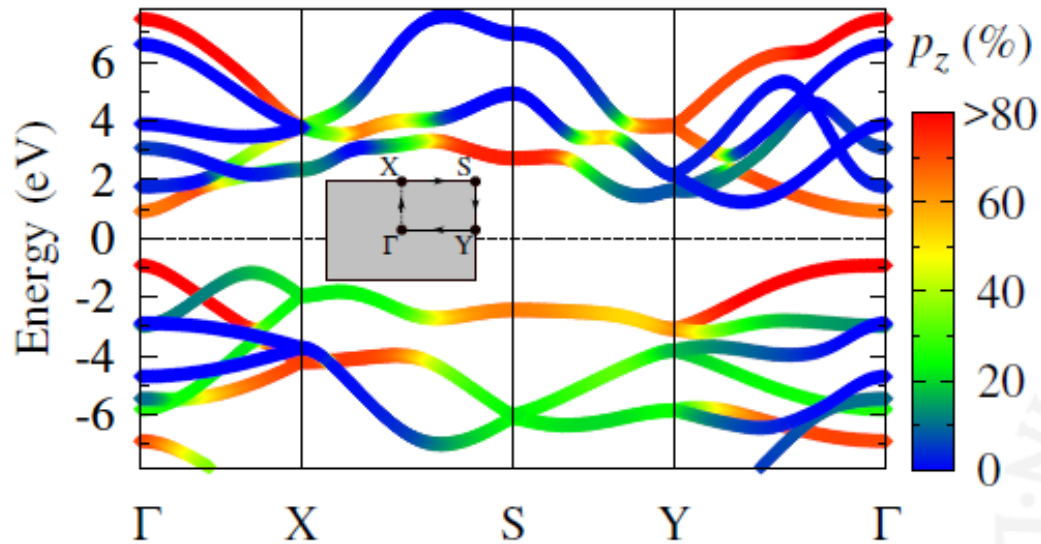
GW is qualitatively important also for single layer



GW predicts a *direct* band gap

Mapping on tight binding model

Single layer BP



- Valence and conduction band edges are isolated
- ...and have predominantly p_z character

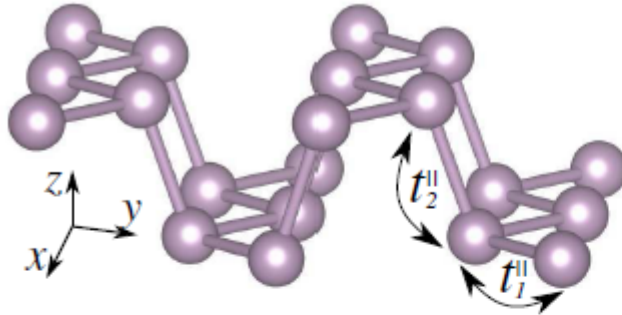
$H_{GW}^{\mathbf{k}}$
*multiorbital
Hamiltonian*



$H_{TB}^{\mathbf{R}}$
*single-orbital
Hamiltonian*

Mapping on tight binding model II

Minimal model for single-layer BP (phosphorene)

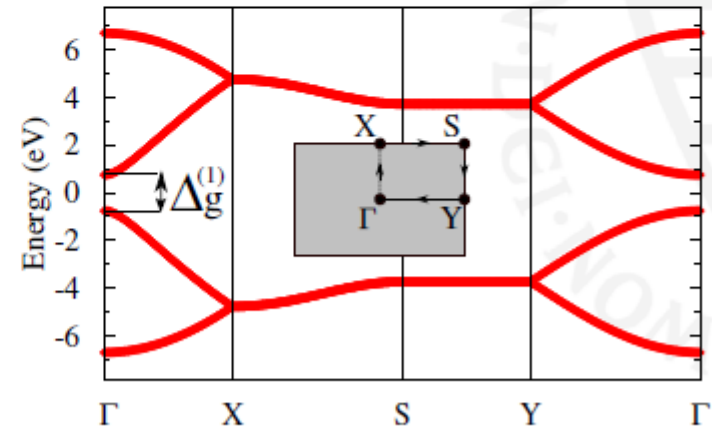


$$t_1^{\parallel} \approx -1.5 \text{ eV} ; t_2^{\parallel} \approx +3.7 \text{ eV}$$

$$H = \sum_{i \neq j} t_{ij}^{\parallel} c_i^{\dagger} c_j$$

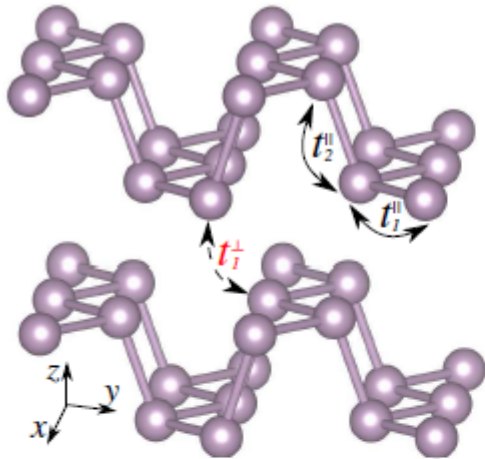
$$\underbrace{\Delta_g^{(1)}(\Gamma)}_{\text{Band gap}} \approx 2t_2^{\parallel} + 4t_1^{\parallel}$$

Band gap appearance
criterion: $t_2^{\parallel} > 2|t_1^{\parallel}|$



Mapping on tight binding model III

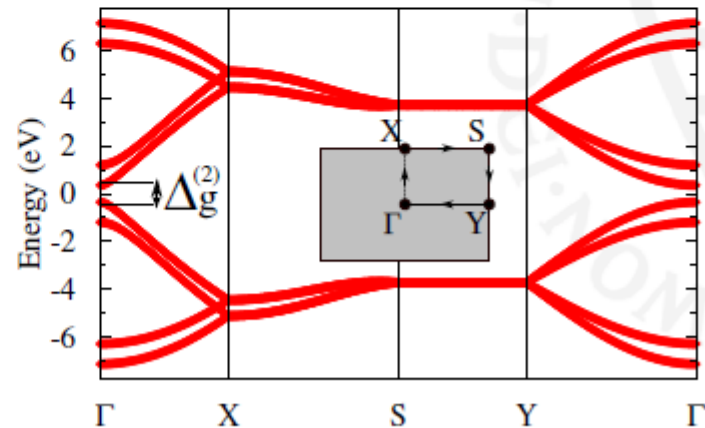
Minimal model for bilayer BP



$$H = \underbrace{\sum_{i \neq j} t_{ij}^{\parallel} c_i^{\dagger} c_j}_{\text{intralayer term}} + \underbrace{\sum_{i \neq j} t_{ij}^{\perp} c_i^{\dagger} c_j}_{\text{interlayer term}}$$

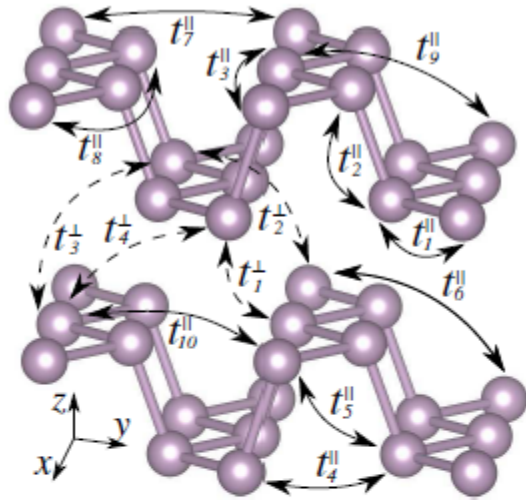
$$t_1^{\parallel} \approx -1.5\text{eV} ; t_2^{\parallel} \approx +3.7\text{eV} ; t_1^{\perp} \approx 0.5\text{eV}$$

t_1^{\perp} accounts for the narrowing of a gap in multilayer BP



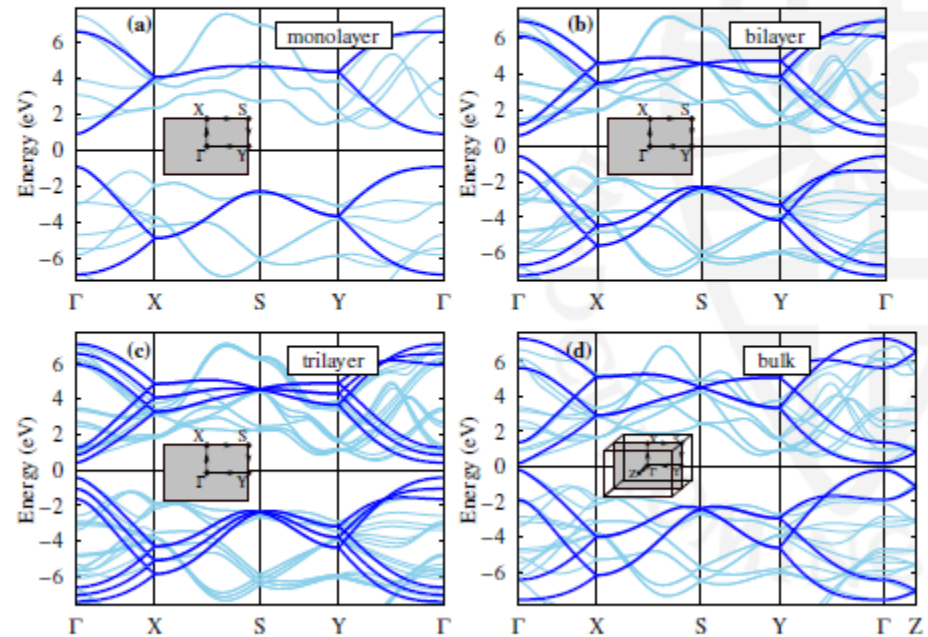
Mapping on tight binding model IV

Optimal TB model for multilayer BP vs GW



$$H = \sum_{i \neq j} t_{ij}^{\parallel} c_i^{\dagger} c_j + \sum_{i \neq j} t_{ij}^{\perp} c_i^{\dagger} c_j$$

- Perfect agreement with GW in low-energy region
- Applicability to BP with arbitrary number of layers



Mapping on tight binding model V

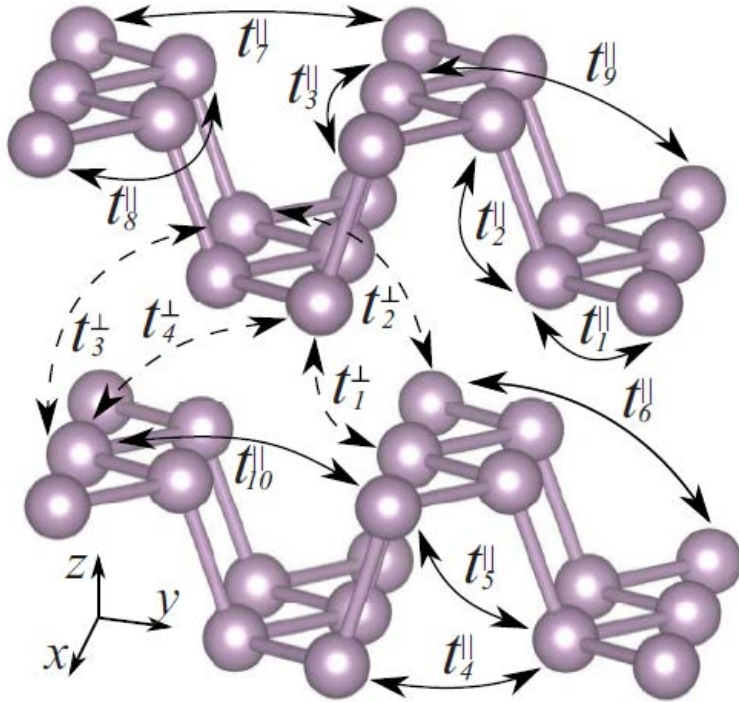
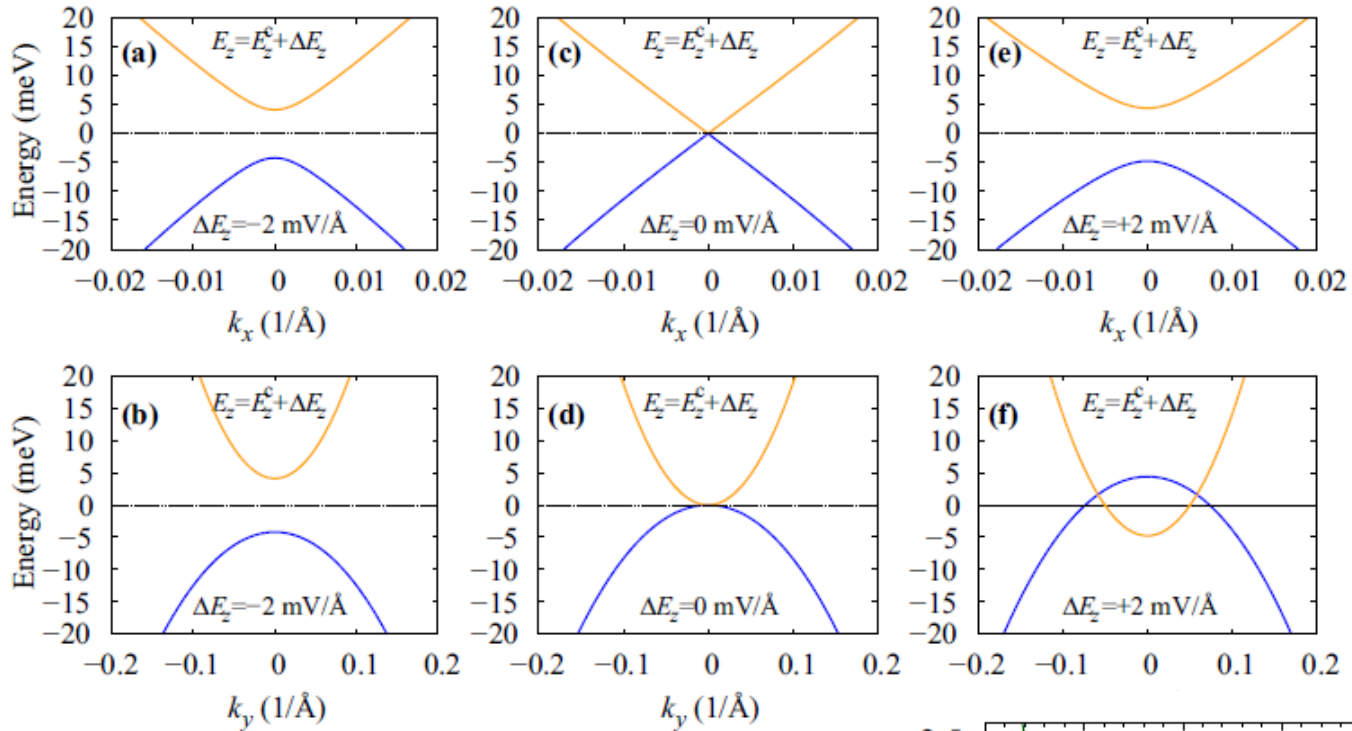


TABLE II. Intralayer (t^{\parallel}) and interlayer (t^{\perp}) hopping parameters (in eV) obtained in terms of the TB Hamiltonian [Eq. (1)] for multilayer BP. d and N_c denote the distances between the corresponding interacting lattice sites and coordination numbers for the given distance, respectively. The hoppings are schematically shown

Intralayer			Intralayer			Interlayer					
No.	t^{\parallel} (eV)	d (Å)	N_c	No.	t^{\parallel} (eV)	d (Å)	N_c	No.	t^{\perp} (eV)	d (Å)	N_c
1	-1.486	2.22	2	6	0.186	4.23	1	1	0.524	3.60	2
2	3.729	2.24	1	7	-0.063	4.37	2	2	0.180	3.81	2
3	-0.252	3.31	2	8	0.101	5.18	2	3	-0.123	5.05	4
4	-0.071	3.34	2	9	-0.042	5.37	2	4	-0.168	5.08	2
5	-0.019	3.47	4	10	0.073	5.49	4	5	0.000	5.44	1

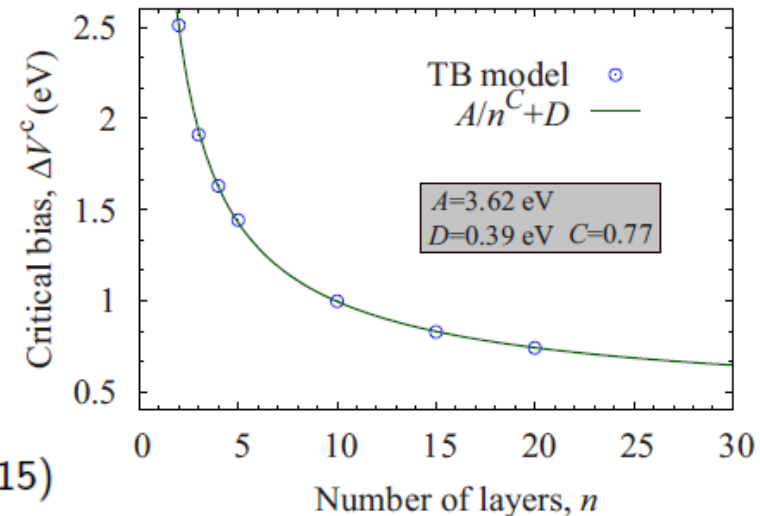
The main difference with graphene: a very large and positive second-neighbour hopping in plane; interlayer hopping is roughly of the same order of magnitude

Effect of interlayer bias: anisotropic Dirac cones

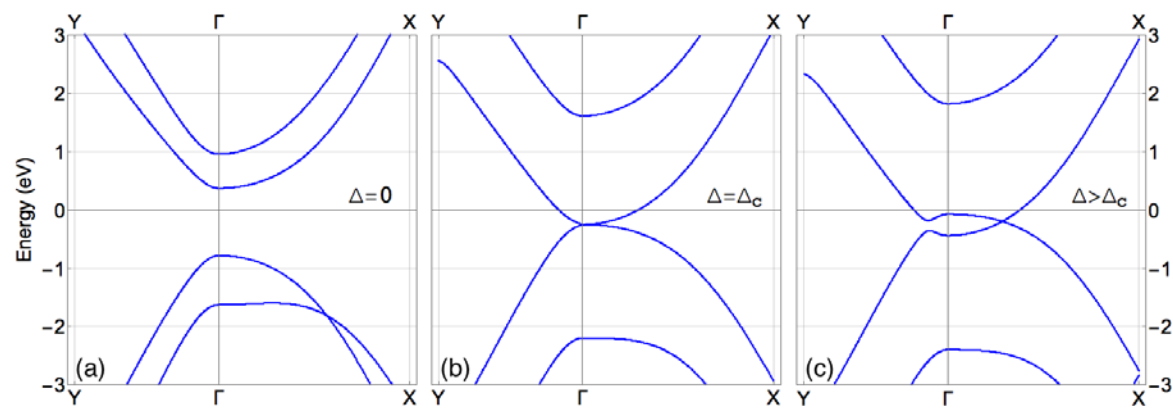


Linear crossing in x direction and parabolic in y direction

Bias leads to gap opening and formation of anisotropic conical points

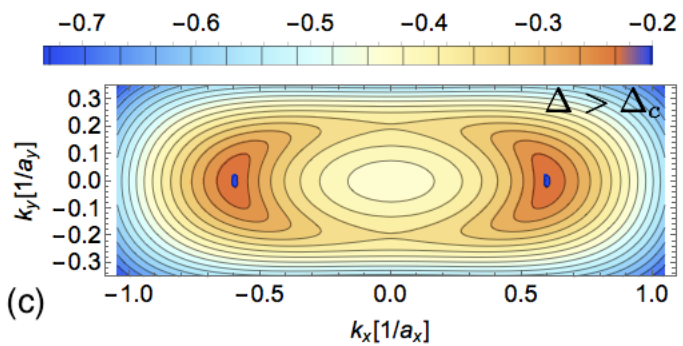
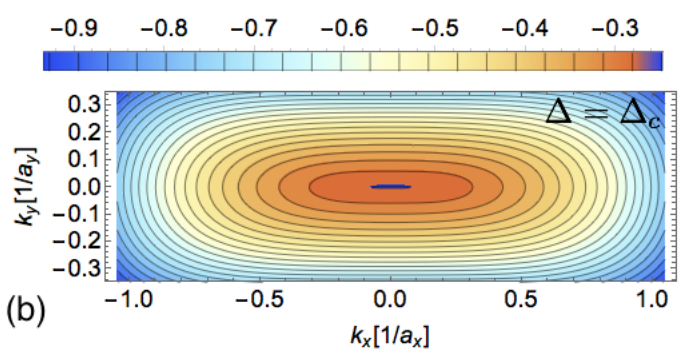
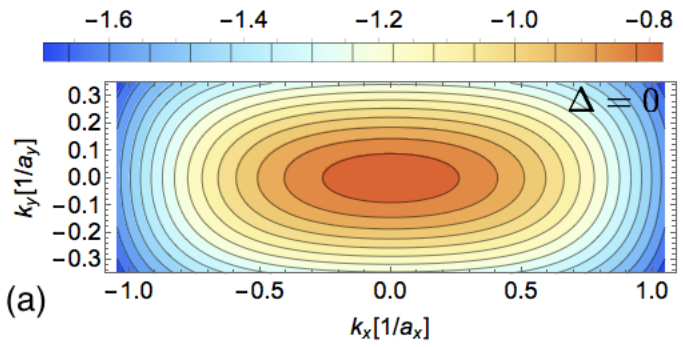


Effect of interlayer bias: anisotropic Dirac cones II



Insulator-semimetal transition with formation of Anisotropic Dirac cones

S. Yuan, MIK, R. Roldan, PRB 93, 245433 (2016)



Experiment: K deposit

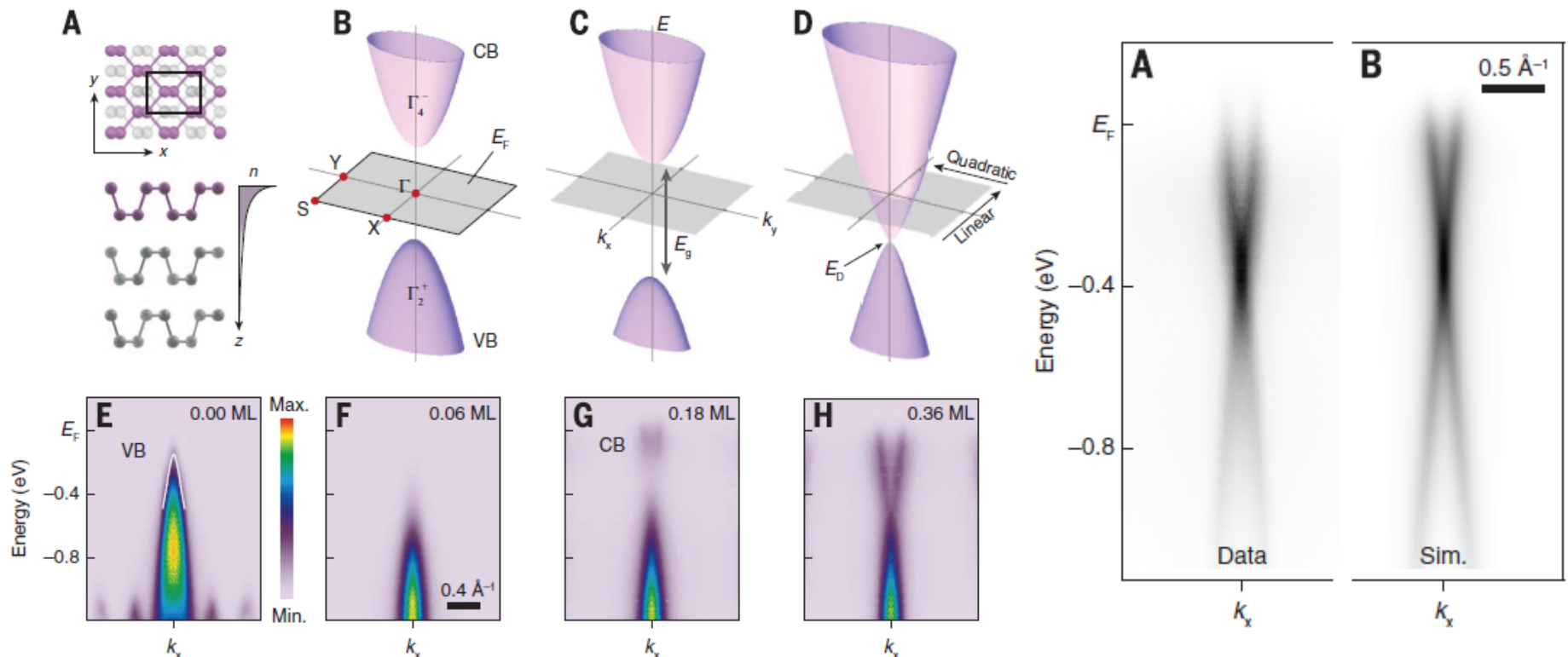
Observation of tunable band gap and anisotropic Dirac semimetal state in black phosphorus

SCIENCE

14 AUGUST 2015 • VOL 349 ISSUE 6249 723

Jimin Kim,¹ Seung Su Baik,^{2,3} Sae Hee Ryu,^{1,4} Yeongsup Sohn,^{1,4} Soohyung Park,²
Byeong-Gyu Park,⁵ Jonathan Denlinger,⁶ Yeonjin Yi,²
Hyoung Joon Choi,^{2,3} Keun Su Kim^{1,4*}

ARPES

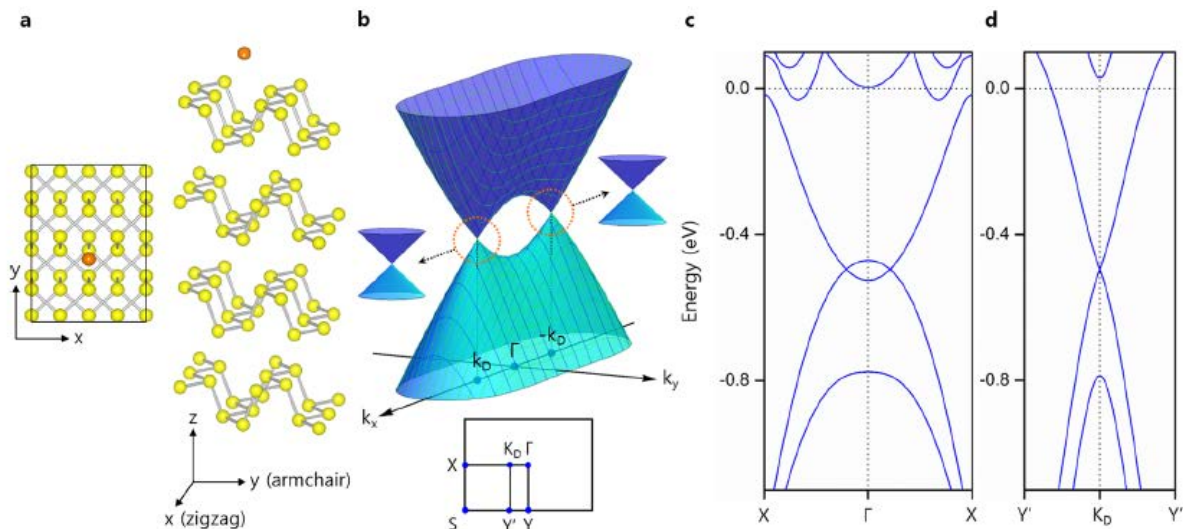
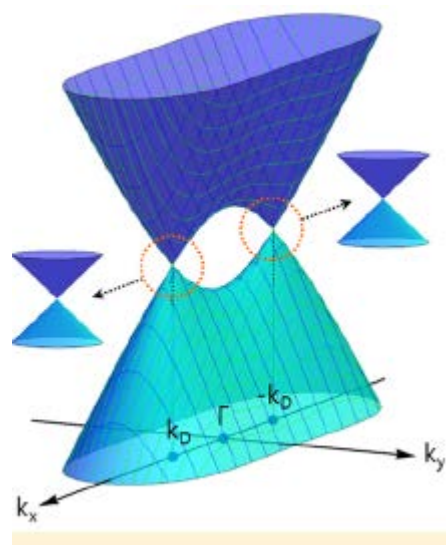


Calculations: K deposit

Emergence of Two-Dimensional Massless Dirac Fermions, Chiral Pseudospins, and Berry's Phase in Potassium Doped Few-Layer Black Phosphorus

DOI: 10.1021/acs.nanolett.5b04106
Nano Lett. 2015, 15, 7788–7793

Seung Su Baik,^{†,‡} Keun Su Kim,^{§,||} Yeonjin Yi,[†] and Hyoung Joon Choi^{*,†,‡}



Indeed, very similar to just perpendicular electric field effect

High-frequency laser fields

Quickly oscillating strong electric field means quickly oscillating effective hopping

$$t_{ij} \rightarrow t_{ij} \exp \left\{ \frac{ie}{\hbar c} \int_{\vec{R}_j}^{\vec{R}_i} d\vec{r}' \vec{A}(\vec{r}', t) \right\}$$

At very high frequency effective *static* Hamiltonian should exist

Classical analog: Kapitza pendulum



One needs to develop efficient perturbative theory in inverse frequency of the laser field

In classical mechanics: Bogoliubov, Krylov ...

Development for matrix Hamiltonians:
A. P. Itin & A. I. Neishtadt, *Phys. Lett. A*
378, 822 (2014)

Laser-induced topological transitions

C. Dutreix, E. A. Stepanov & MIK, Phys. Rev. B 93, 241404(R) (2016)

In bilayer, electric bias creates insulator-semimetal transition; but with high-frequency laser field one can make it for the single layer

Averaging over high-frequency field:

A. P. Itin & MIK, Phys. Rev. Lett. 115, 075301 (2015)

C. Dutreix & MIK, Phys. Rev. B 95, 024306 (2017)

High-frequency expansion (in $1/\Omega$) for the effective *static* Hamiltonian

$$\tilde{H}_1 = H_0, \quad \tilde{H}_2 = -\frac{1}{2} \sum_{m \neq 0} \frac{[H_m, H_{-m}]}{m},$$

$$\tilde{H}_3 = \frac{1}{2} \sum_{m \neq 0} \frac{[[H_m, H_0], H_{-m}]}{m^2} + \frac{1}{3} \sum_{m \neq 0} \sum_{n \neq 0, m} \frac{[[H_m, H_{n-m}], H_{-n}]}{mn},$$

$$H_m = \int_{-\pi}^{+\pi} \frac{d\tau}{2\pi} e^{im\tau} H(\tau)$$

Very important: NN and NNN hopping are renormalized differently, and both are very relevant for the electronic structure!

Laser-induced topological transitions II

Single-particle Hamiltonian (only bands), Peierls substitution

$$\mathbf{A}(t) = (A_x \cos \Omega t, A_y \sin[\Omega t - \phi], 0)$$

Second-order effective static Hamiltonian

On can pass from band insulator to topological insulator or to semimetal

Elliptic polarization: topological insulator

Linear polarization: semimetal, no gap

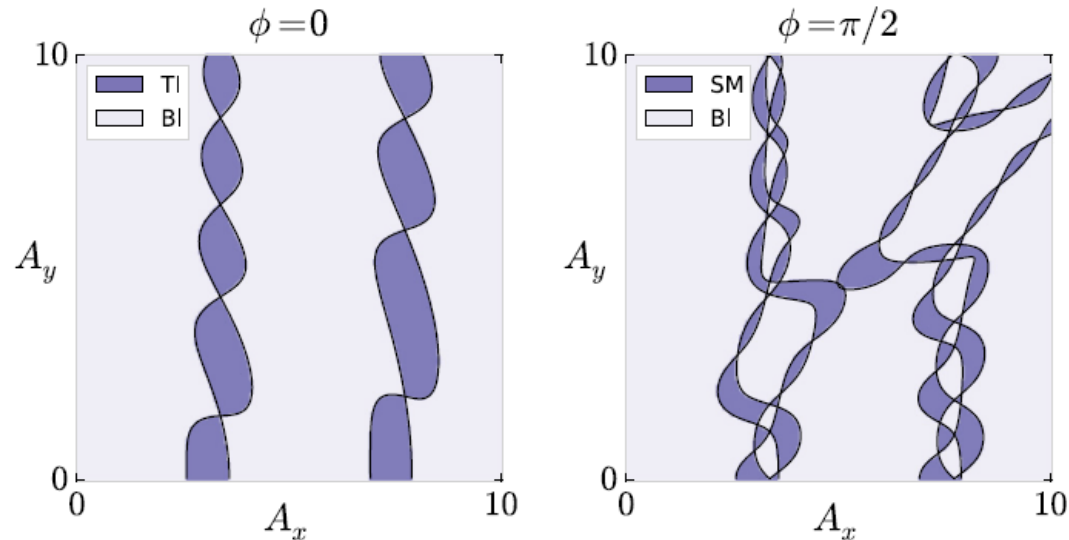
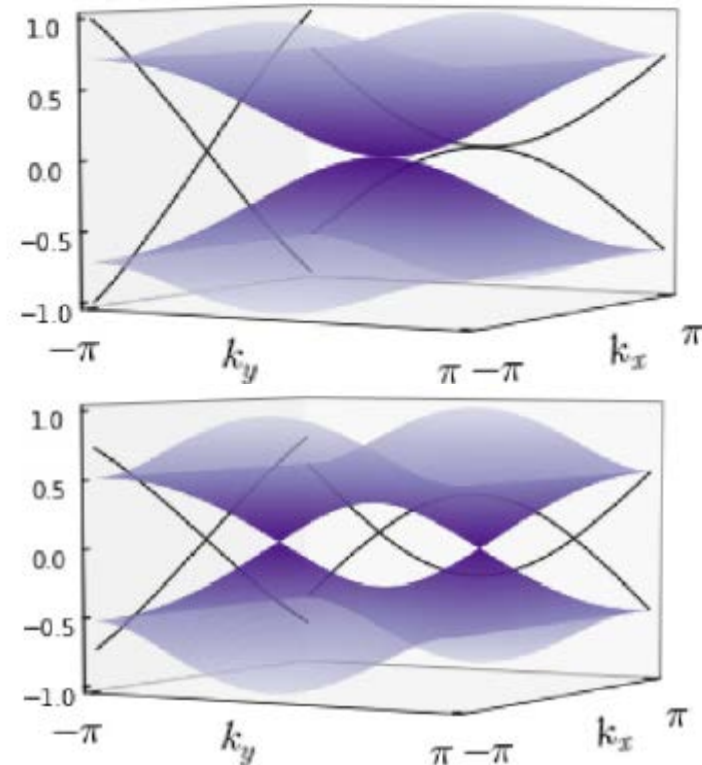


FIG. 3. Phase diagrams for electric fields with elliptic (left) and linear (right) polarizations. Light purple areas refer to band insulating (BI) phases characterized by $e^{i\gamma c} = +1$. Dark purple areas correspond to semimetallic (SM) and topological insulating (TI) phases in which $e^{i\gamma c} = -1$. Components A_x and A_y are given in \AA^{-1} .

Lowest-energy bands in semimetallic phase



Optics

Two approaches for $\sigma_{xx}(\omega)$:

① **k-space** (based on *GW* approximation)

$$\sigma_{\alpha\beta}(\omega) = \frac{i\hbar}{N_k \Omega} \sum_{\mathbf{k}} \sum_{mn} \frac{f_{m\mathbf{k}} - f_{n\mathbf{k}}}{\epsilon_{m\mathbf{k}} - \epsilon_{n\mathbf{k}} - (\hbar\omega + i\eta)} \frac{\langle n\mathbf{k} | j_\alpha | m\mathbf{k} \rangle \langle m\mathbf{k} | j_\beta | n\mathbf{k} \rangle}{\epsilon_{m\mathbf{k}} - \epsilon_{n\mathbf{k}} - (\hbar\omega + i\eta)}$$

② **R-space** (tight-binding propagation method)

$$\sigma_{\alpha\beta}(\omega) = \lim_{\epsilon \rightarrow 0^+} \frac{e^{-\tilde{\beta}\omega} - 1}{\omega \Omega} \int_0^\infty e^{-\epsilon t} \sin \omega t \times 2 \operatorname{Im} \langle \varphi | f(\mathcal{H}) J_\alpha(t) [1 - f(\mathcal{H})] J_\beta | \varphi \rangle dt$$

Chebyshev polynom expansion, etc. – up to 10^9 sites

PHYSICAL REVIEW B 82, 115448 (2010)



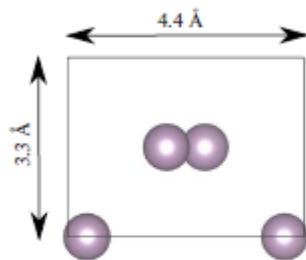
Successfully applied to graphene

Modeling electronic structure and transport properties of graphene with resonant scattering centers

Optics II

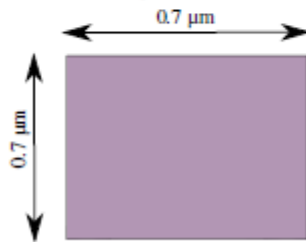
Two approaches for $\sigma_{xx}(\omega)$:

- GW (k-space)



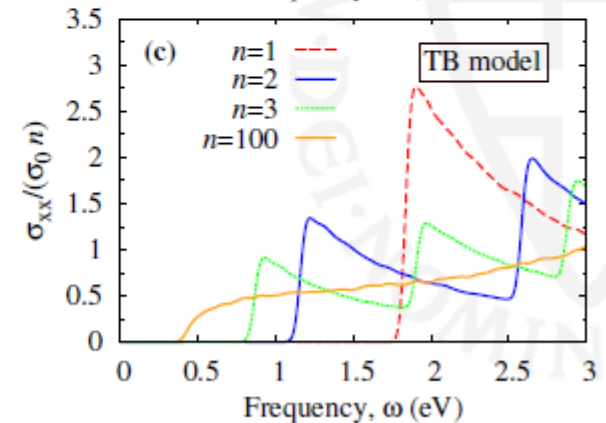
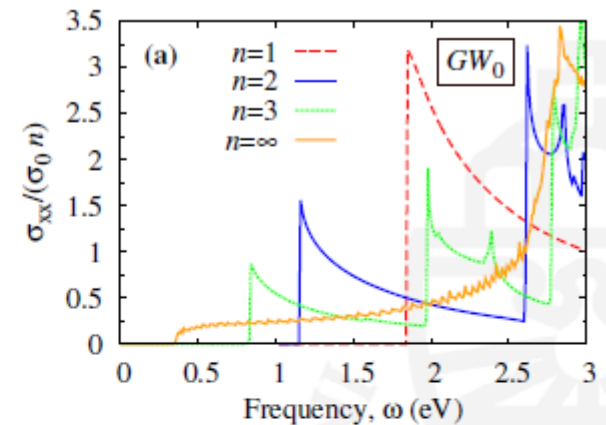
primitive cell
(four atoms)

- TB (R-space)



large supercell
($\sim 10^7$ atoms)

Excellent agreement up to $\omega \sim 2.5$ eV



Hyperbolic plasmons

Just to remind:
crystalloptics

$$\vec{k} = k_0 \vec{n}, \quad k_0 = \frac{\omega}{c} \quad \det \left| n^2 \delta_{ij} - n_i n_j - \varepsilon_{ij}(\omega) \right| = 0$$

$$\varepsilon_{ij}(\omega) = \delta_{ij} + \frac{4\pi i}{\omega} \sigma_{ij}(\omega)$$

Main axes $\varepsilon_{ij} = \varepsilon_i \delta_{ij}$

If $\varepsilon_x \varepsilon_y < 0$

$$\begin{aligned} n_z &= 0 \\ n^2 &= \varepsilon_z \\ \frac{n_x^2}{\varepsilon_y} + \frac{n_y^2}{\varepsilon_x} &= 1 \end{aligned}$$

$$\frac{k_x^2}{|\varepsilon_y|} = \frac{k_y^2}{|\varepsilon_x|}, \quad k \gg k_0 \quad (c \rightarrow \infty)$$

Hyperbolic plasmons

Hyperbolic plasmons in black P

E. Van Veen, A. Nemilentsau, A. Kumar, R. Roldan, MIK, T. Low, S. Yuan, arXiv:1812.03062

Black P is anisotropic – one can find the region where $\varepsilon_x \varepsilon_y < 0$

Manipulations by strain

$$t_{ij}(\mathbf{r}_{ij}) = t_{ij}(\mathbf{r}_{ij}^0) \left(1 - \beta_{ij} \frac{|\mathbf{r}_{ij} - \mathbf{r}_{ij}^0|}{|\mathbf{r}_{ij}^0|} \right)$$

Or by optical gain (nonequilibrium occupation)

Quasi-equilibrium distribution

$$n_F(E) = \theta(E) f\left(E + \frac{E_g}{2} + \Delta\mu\right) + \theta(-E) f\left(E - \frac{E_g}{2} - \Delta\mu\right)$$

$$f(E - \mu) = \frac{1}{e^{(E-\mu)/kT} + 1} \quad T = 300 \text{ K}$$

Hyperbolic plasmons in black P II

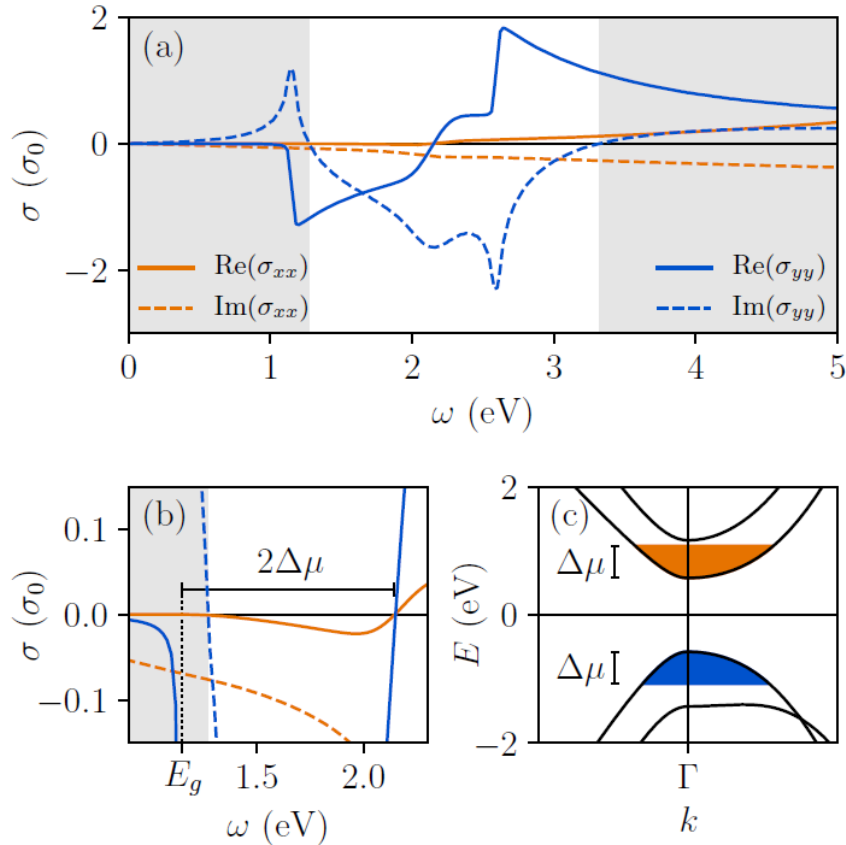


FIG. 2. (a) The optical conductivity of bilayer black phosphorus with photo-doping $\Delta\mu = 0.5$ eV. (b) A close-up of the region where $\text{Re}(\sigma_{yy}) < 0$, showing a new hyperbolic region (shaded) for $\omega < 1.27$ eV. (c) The corresponding band structure around the Γ -point, with the population-inverted pockets shown in blue and orange.

$$\sigma_0 = \frac{\pi e^2}{2h}$$

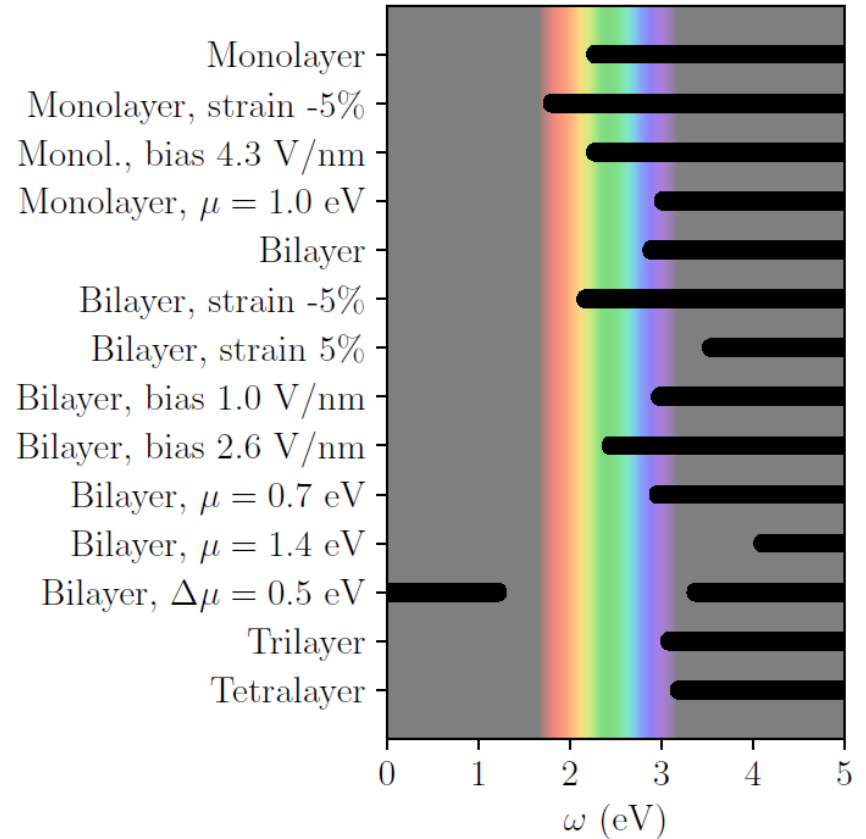
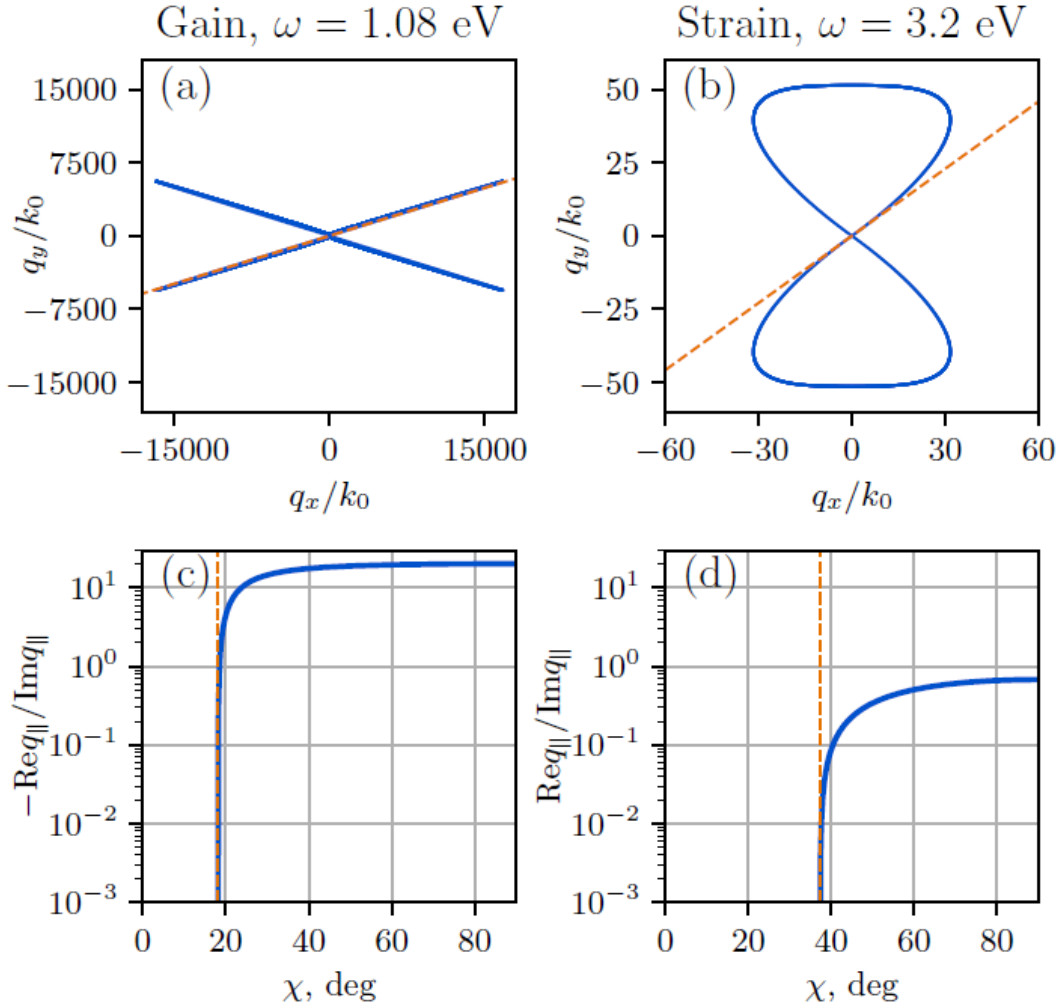


FIG. 3. The hyperbolic region (indicated in black lines) for different tuning parameters. The visual spectrum is indicated in color.

One can manipulate black (hyperbolic) regions

Hyperbolic plasmons in black P III



Strong deviations from hyperbolicity in the case of strain due to quite strong damping

$$q_{\parallel}^2 = \gamma^2 + k_0^2,$$

$$\gamma = \frac{ik_0}{2\sigma_{\mathbf{q}\mathbf{q}}} \left[\left(\frac{2}{\eta_0} + \frac{\eta_0}{2} \sigma_{xx} \sigma_{yy} \right) + \sqrt{\left(\frac{2}{\eta_0} + \frac{\eta_0}{2} \sigma_{xx} \sigma_{yy} \right)^2 - 4\sigma_{\mathbf{q}\mathbf{q}} \sigma_{\perp\perp}} \right]$$

$$\sigma_{\mathbf{q}\mathbf{q}}(\chi) = \sigma_{xx} \cos^2 \chi + \sigma_{yy} \sin^2 \chi,$$

$$\sigma_{\perp\perp}(\chi) = \sigma_{xx} \sin^2 \chi + \sigma_{yy} \cos^2 \chi.$$

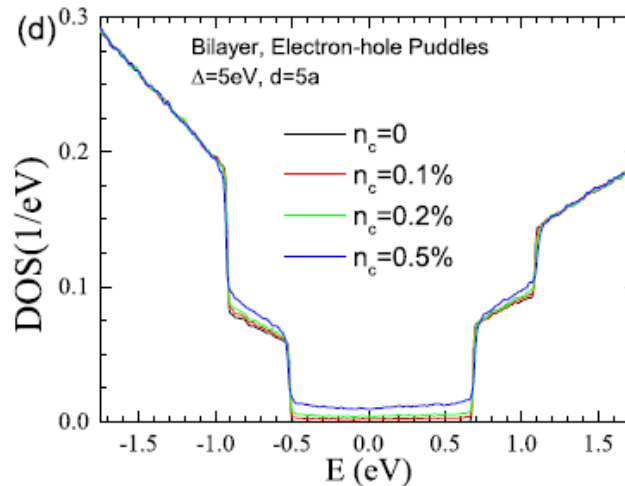
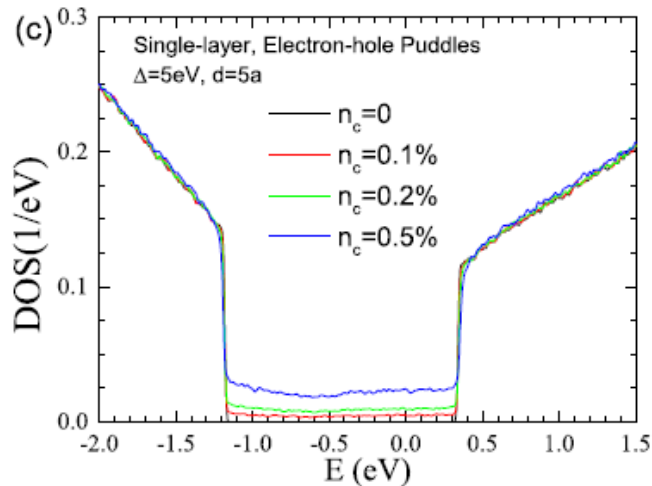
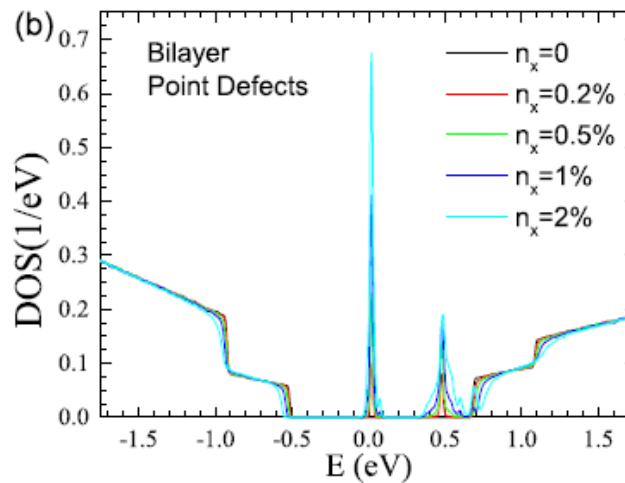
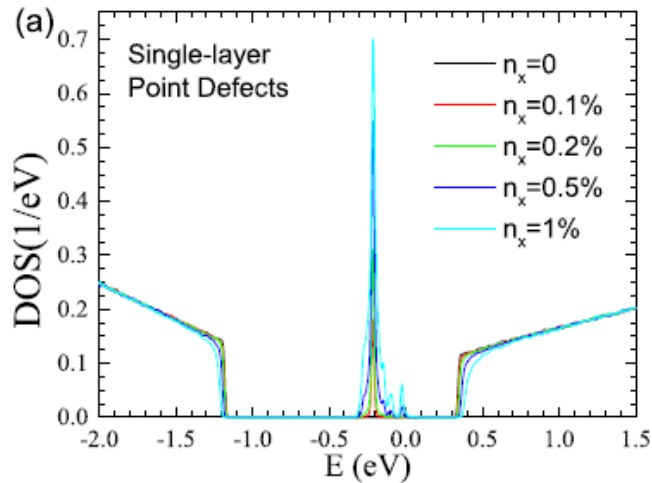
FIG. 4. Iso-frequency contours and figures of merit for hyperbolic materials with gain ($\Delta\mu = 0.5$ eV) and strain ($\epsilon_{yy} = -5\%$), calculated using Eq. (10). The hyperbola asymptotes (orange dashed lines) are defined using Eq. (14).

Large scale TB simulations for disordered BP

PHYSICAL REVIEW B 91, 115436 (2015)

Transport and optical properties of single- and bilayer black phosphorus with defects

Shengjun Yuan,* A. N. Rudenko, and M. I. Katsnelson



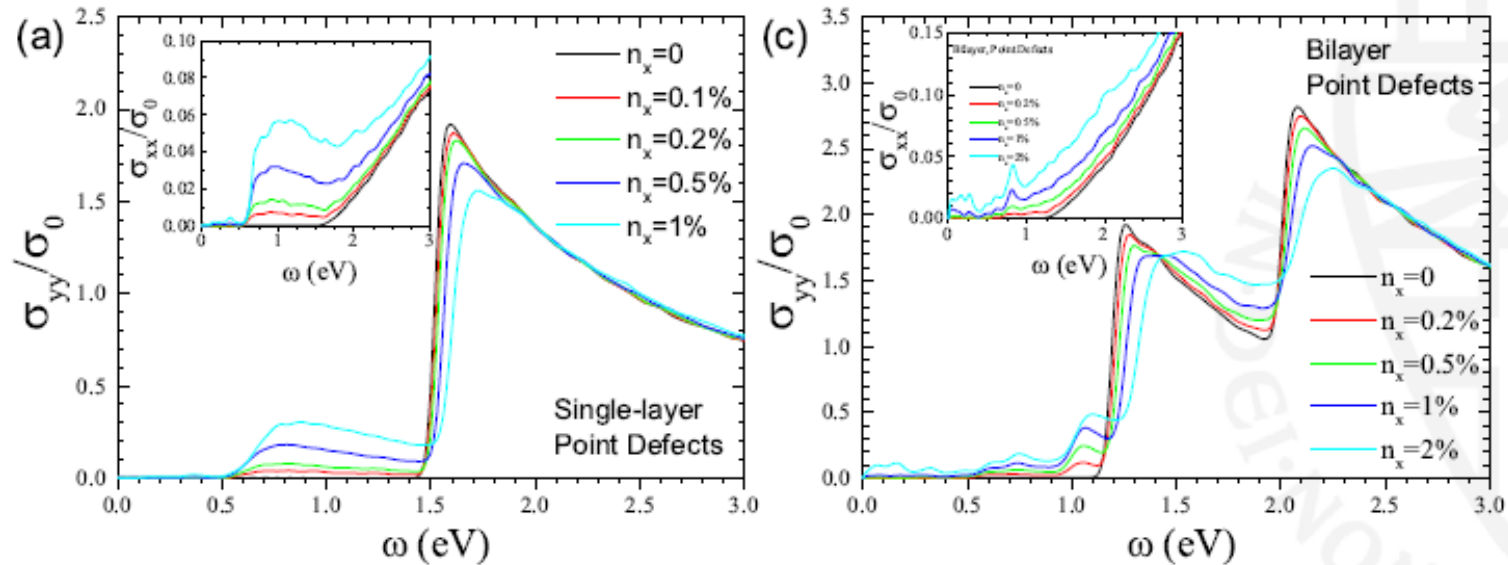
Point defects: missing atoms

Puddles: Gaussian electrostatic potential

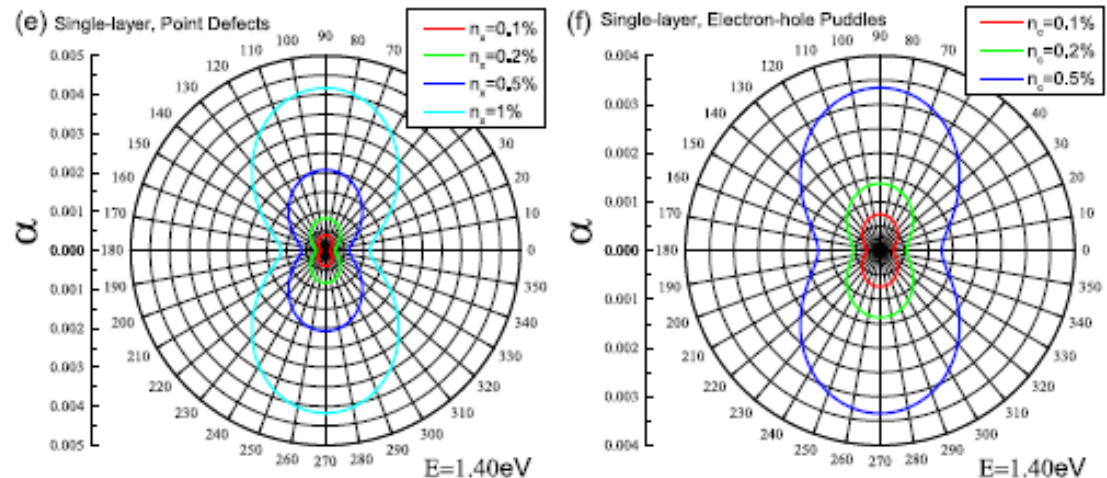
$$v_i = \sum_{k=1}^{N_{\text{imp}}^v} U_k \exp\left(-\frac{|\mathbf{r}_i - \mathbf{r}_k|^2}{2d^2}\right)$$

Large scale TB simulations for disordered BP II

Optical conductivities in monolayer and bilayer BP



Anisotropy of optical adsorption

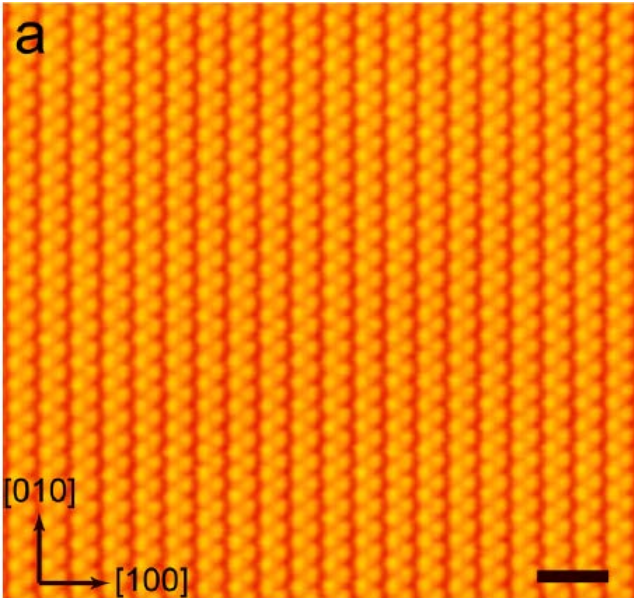


STM observation of vacancy states

NANO LETTERS

Probing Single Vacancies in Black Phosphorus at the Atomic Level

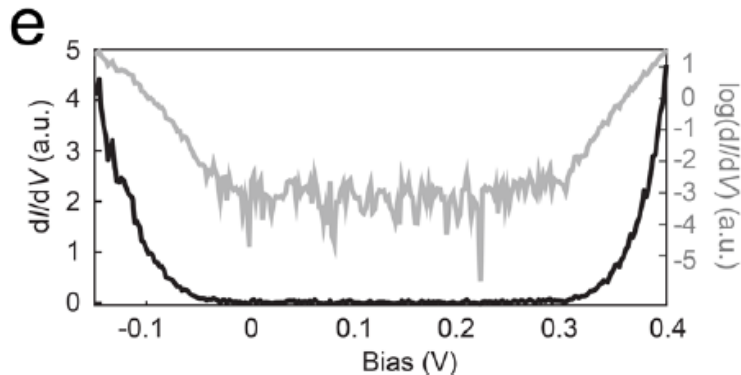
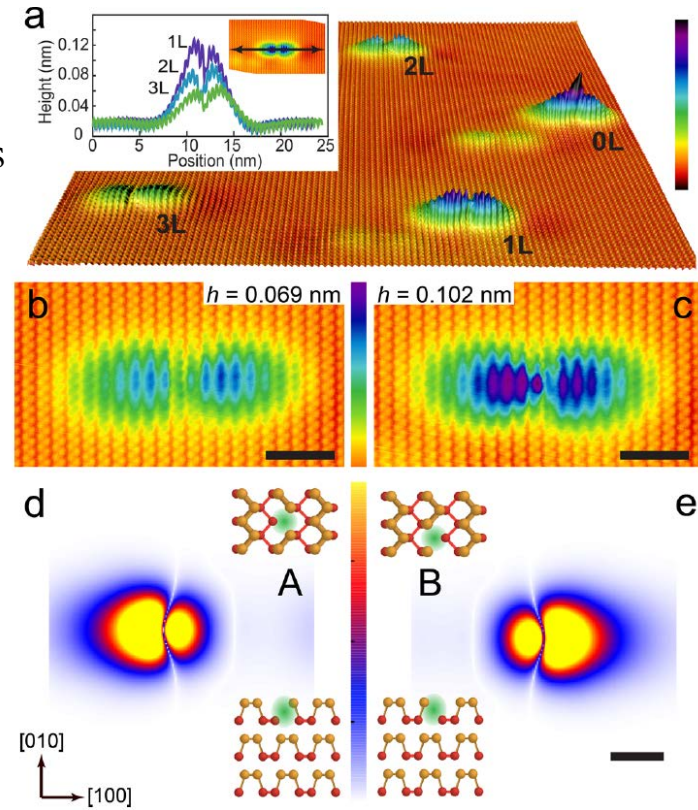
Brian Kiraly, Nadine Hauptmann, Alexander N. Rudenko, Mikhail I. Katsnelson, and Alexander A. Khajetoorians*



STM image of bulk black P – atomically flat surface

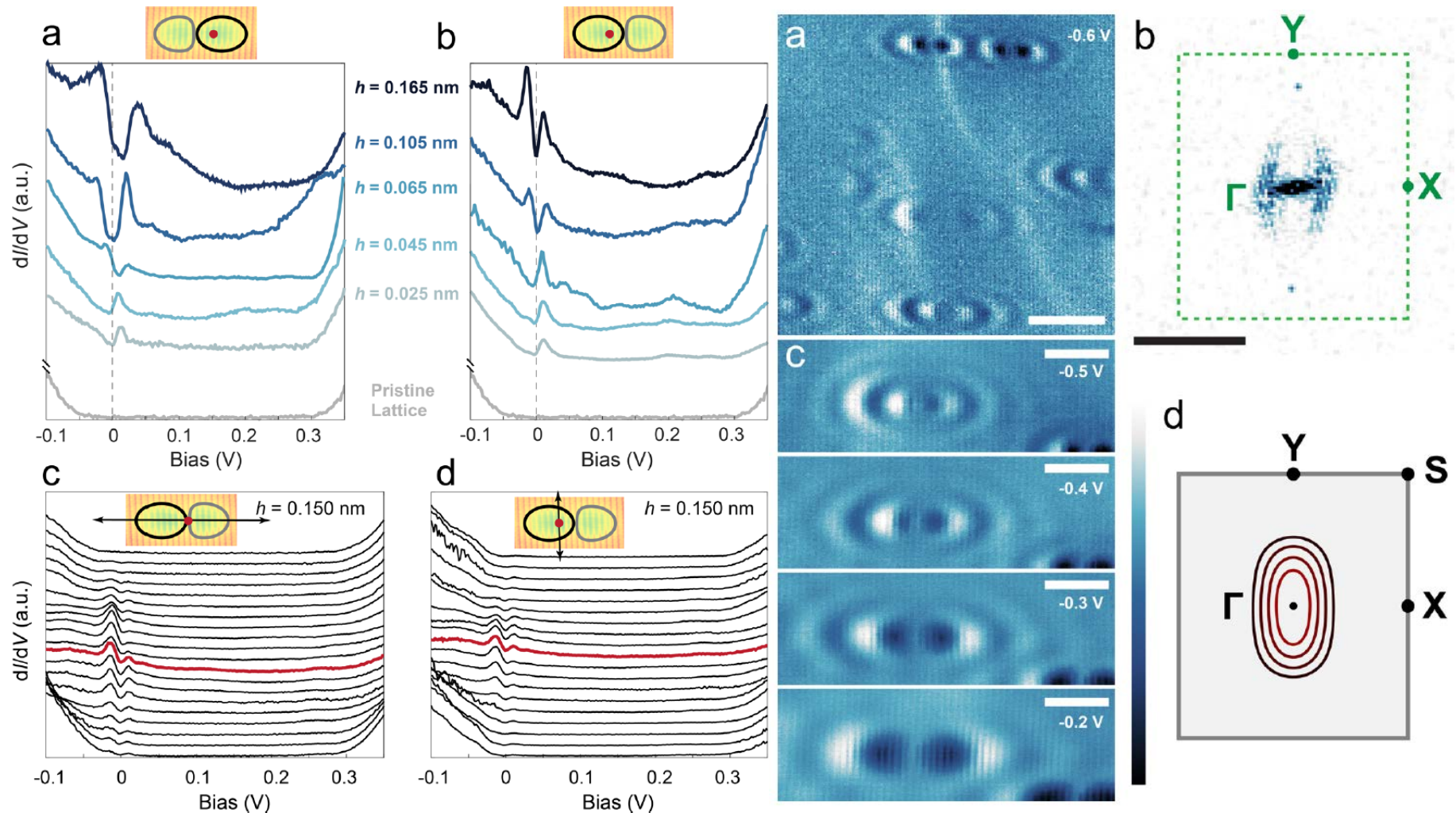
Comparison with calculations allows to attribute peaks to vacancies

Figure 2. (a) Three-dimensional representation of a constant-current STM image with a distribution of single vacancies in black phosphorus ($V_S = -0.1$ V, $I_t = 200$ pA, size = 62 nm \times 48 nm, color bar = 0–0.2 nm). (Inset) Line profiles taken across the vacancies labeled 1L, 2L, and 3L in (a). Constant-current STM image of a single vacancy at (b) sublattice A and (c) at sublattice B ($V_S = -0.1$ V, $I_t = 200$ pA, scale bar = 2 nm). (d) Tight-binding calculations of the charge density of a single vacancy in black phosphorus located at (d) sublattice site A and (e) sublattice site B (scale bar = 1 nm).



Gap 0.32 eV

STM observation of vacancy states II



Vacancies in sublattice A and B, first and second layers

Friedel oscillations around vacancies

Co atom at black-P surface

ARTICLE

DOI: 10.1038/s41467-018-06337-4

OPEN

NATURE COMMUNICATIONS | (2018)9:3904

An orbitally derived single-atom magnetic memory

Brian Kiraly¹, Alexander N. Rudenko^{1,2,3}, Werner M.J. van Weerdenburg¹, Daniel Wegner¹, Mikhail I. Katsnelson¹ & Alexander A. Khajetoorians¹

Several metastable configurations of Co atom, switching between them is possible between two states of hollow sites (top site is separated from them)

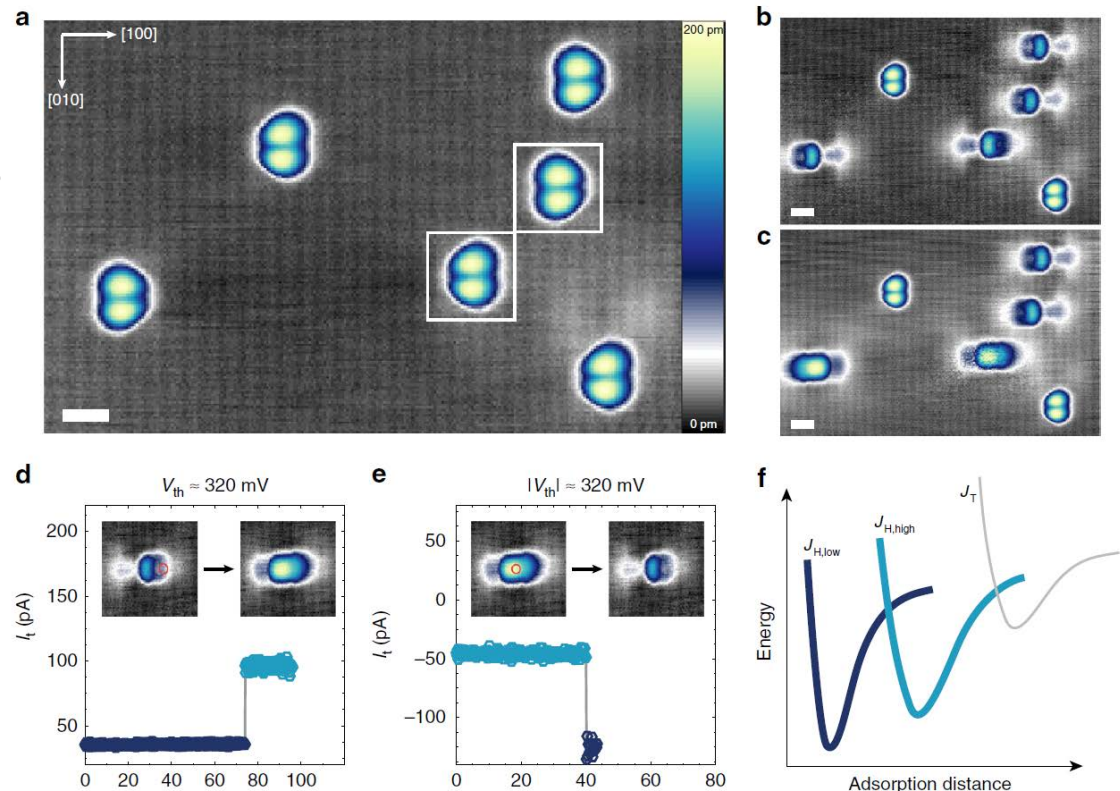
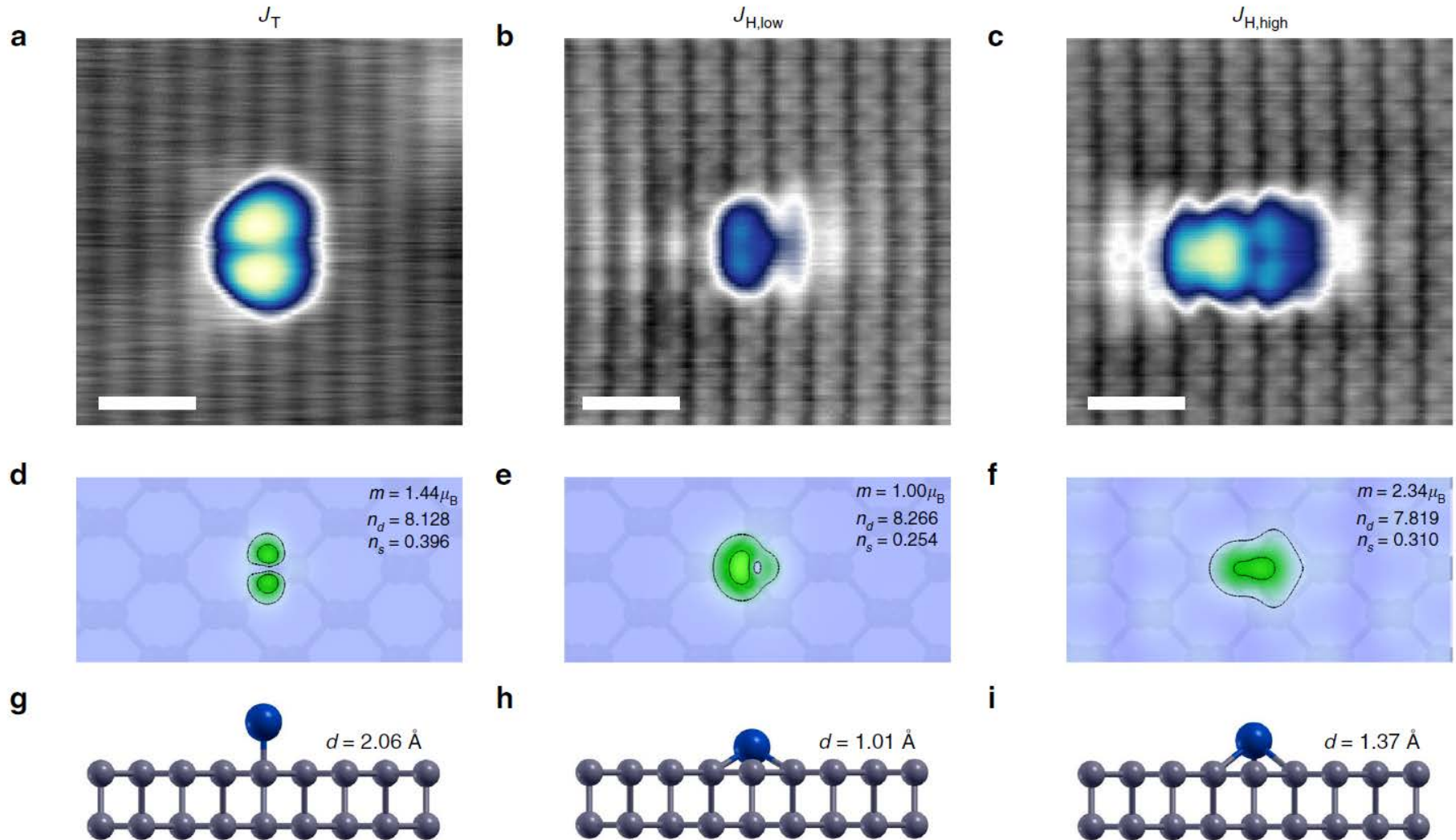


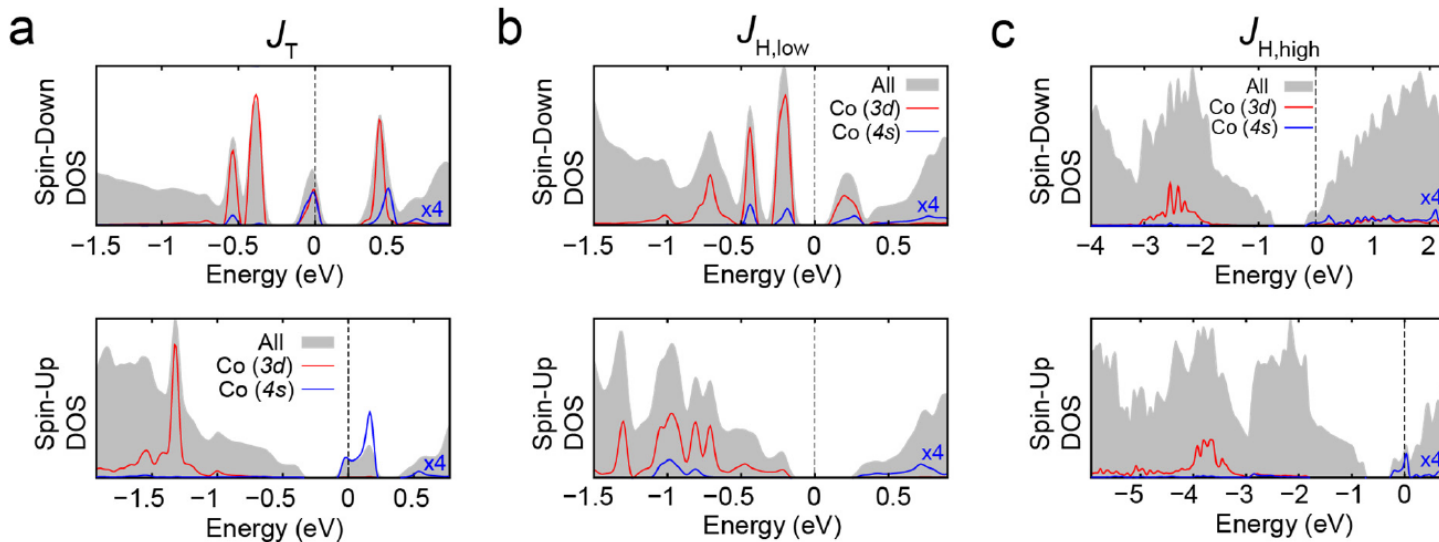
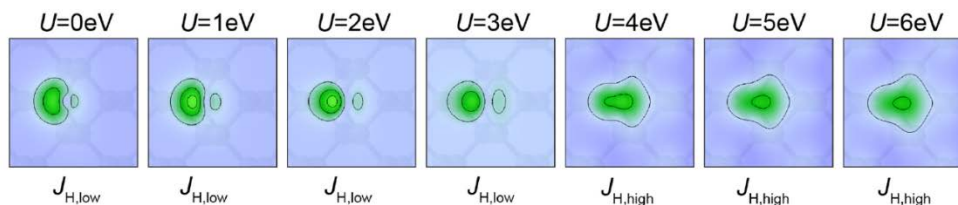
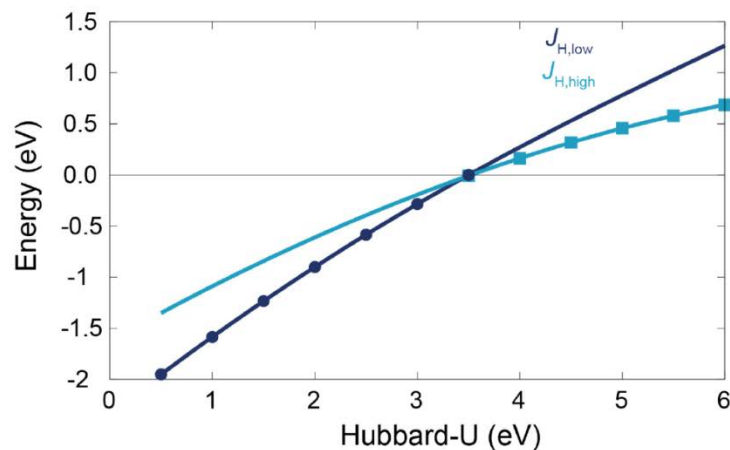
Fig. 1 Adsorption and switching of Co on BP. **a** Six Co species on BP as deposited at $T < 5$ K ($V_s = -400$ mV, $I_t = 20$ pA, scale bar = 1 nm). Boxed atoms show species related through mirror plane along [010]. **b** Four atoms from **a** have been switched into $J_{H,low}$ ($V_s = -400$ mV, $I_t = 20$ pA, scale bar = 1 nm). **c** Two atoms from **b** have been switched into $J_{H,high}$ ($V_s = -400$ mV, $I_t = 20$ pA, scale bar = 1 nm). **d** Switching characteristics from $J_{H,low}$ to $J_{H,high}$ with $V_s = 420$ mV and **e** $J_{H,high}$ to $J_{H,low}$ with $V_s = -680$ mV. Approximate threshold biases for switching (V_{th}) are noted. Orange circles indicate the tip position during the switching sequence. The inset images showing before and after configurations are 4 nm \times 4 nm in size. **f** Schematic representation of adsorption energy curves for Co species on BP

Co atom at black-P surface II



DFT+U calculations ($U = 4 \text{ eV}$) confirm two metastable states for Co in hollow site

Co atom at black-P surface III



Plasmons: role of defects

PHYSICAL REVIEW B 92, 115440 (2015)

Screening and plasmons in pure and disordered single- and bilayer black phosphorus

Fengping Jin,¹ Rafael Roldán,^{2,*} Mikhail I. Katsnelson,³ and Shengjun Yuan^{3,†}

Kubo formula,
TB propagation
method

Static screening

X zigzag direction
Y armchair direction

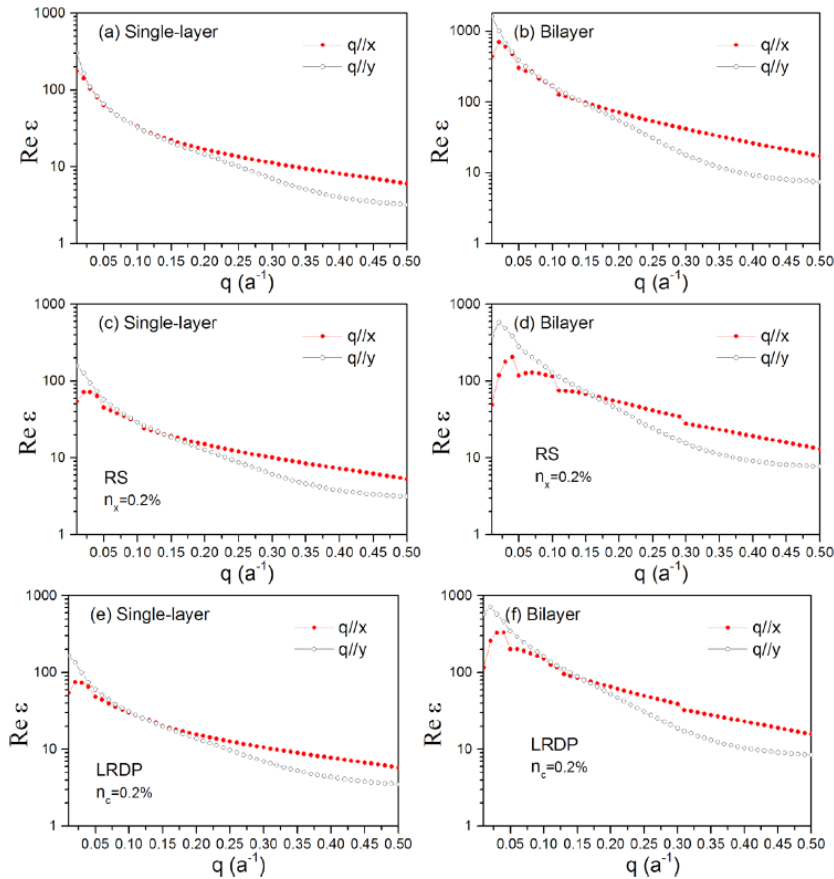


FIG. 2. (Color online) Static dielectric function of single- (left) and bilayer (right) BP. The chemical potential is set to be $\mu = 0.4$ eV for single layer and 0.73 eV for bilayer. The temperature is fixed as the room temperature $T = 300$ K. Plots (a) and (b) correspond to pristine BP, (c) and (d) correspond to samples with resonant scatterers originated from a concentration of $n_x = 0.2\%$ vacant atoms, and (e) and (f) correspond to samples with long-range disorder potential with a concentration of $n_c = 0.2\%$ Gaussian centers.

Plasmons Single Layer II

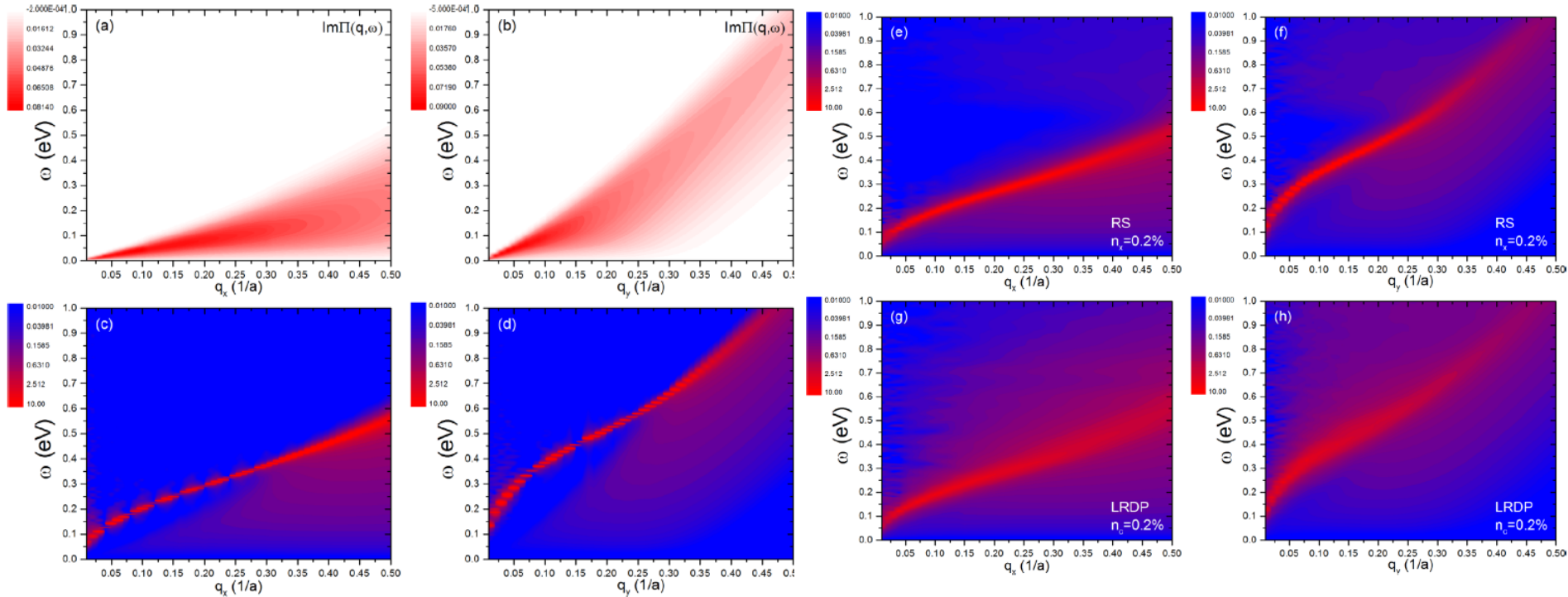


FIG. 3. (Color online) Electron-hole continuum as defined from the noninteracting polarization function (a) and (b), and energy loss functions (c)–(h) of single-layer BP along zigzag (left) and armchair (right) directions. The simulations are done for (a)–(d) pristine BP, (e) and (f) samples with resonant scatterers, and (g) and (h) samples with long-range disorder potentials. All the results are calculated at $T = 300$ K. We notice that the apparent discretization of the spectrum in some of the plots is an artifact due to finite size limitations in our calculations.

Chemical potential ≈ 0.1 eV above the bottom of conduction band (0.4 eV for single layer, 0.73 eV for bilayer)

Plasmons Single Layer III

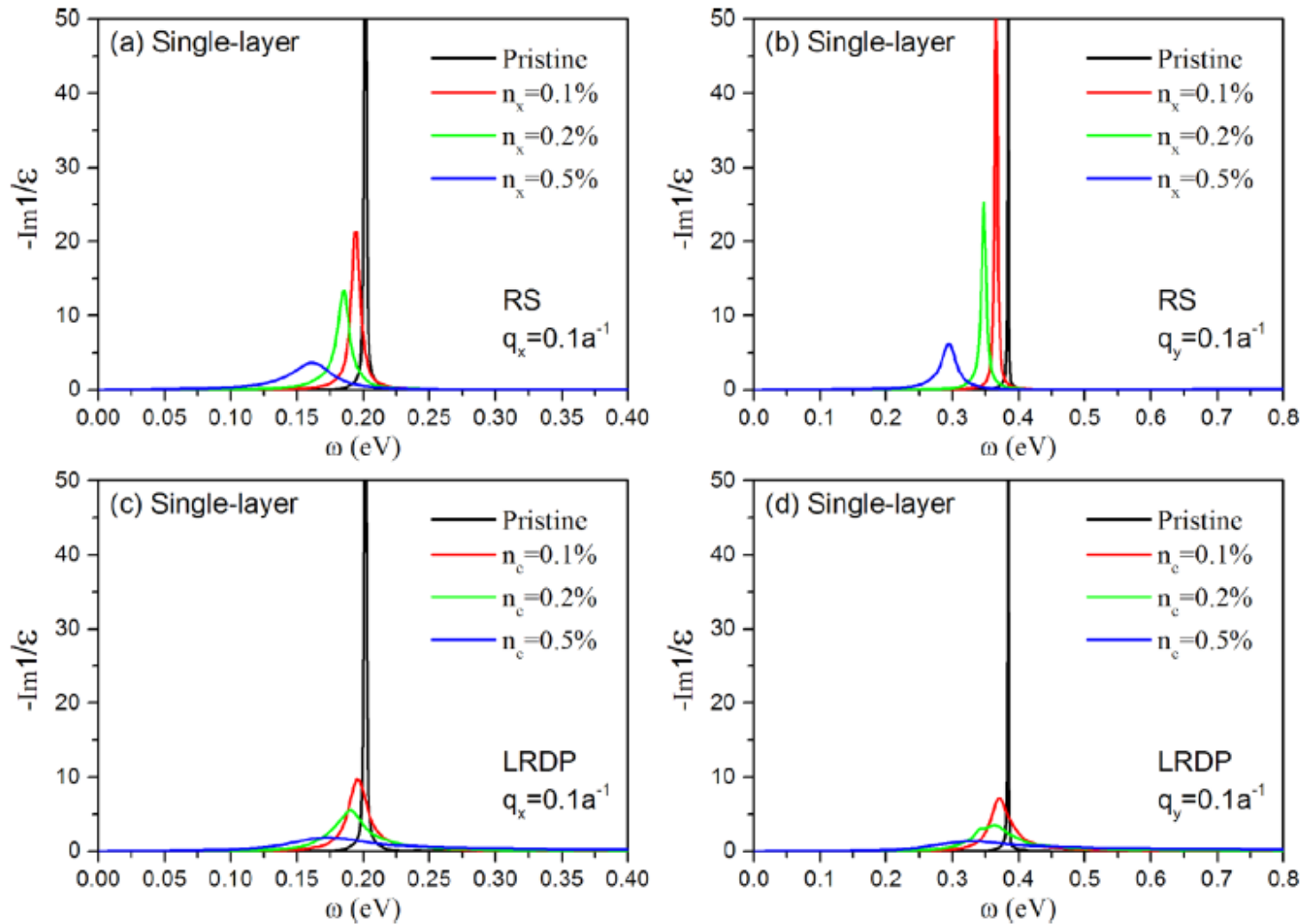


FIG. 4. (Color online) Energy loss functions of single-layer BP along zigzag (left) and armchair (right) directions. Panels (a) and (b) compare the loss function of pristine single-layer BP with that of samples with different concentrations of point defects. Panels (c) and (d) correspond to LRDP. All the results are calculated at $T = 300$ K.

Plasmons: Bilayer

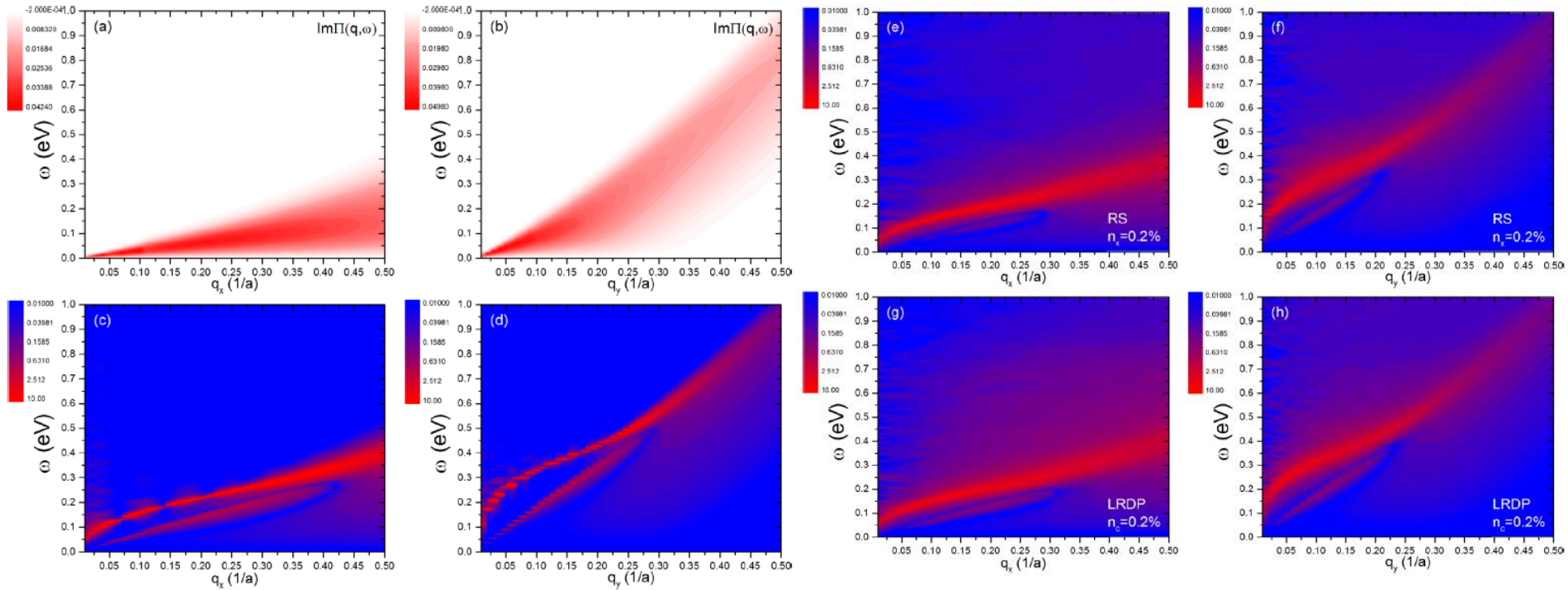


FIG. 6. (Color online) Electron-hole continuum as defined from the noninteracting polarization function (a) and (b), and energy loss functions (c)–(h) of bilayer BP along zigzag (left) and armchair (right) directions. The simulations are done for (a)–(d) pristine bilayer BP, (e) and (f) samples with resonant scatterers, and (g) and (h) samples with long-range disorder potentials. All the results are calculated at $T = 300$ K.

“Acoustic” and “optical” plasmon branches, with square-root and linear dispersion, respectively

Plasmons: Bilayer II

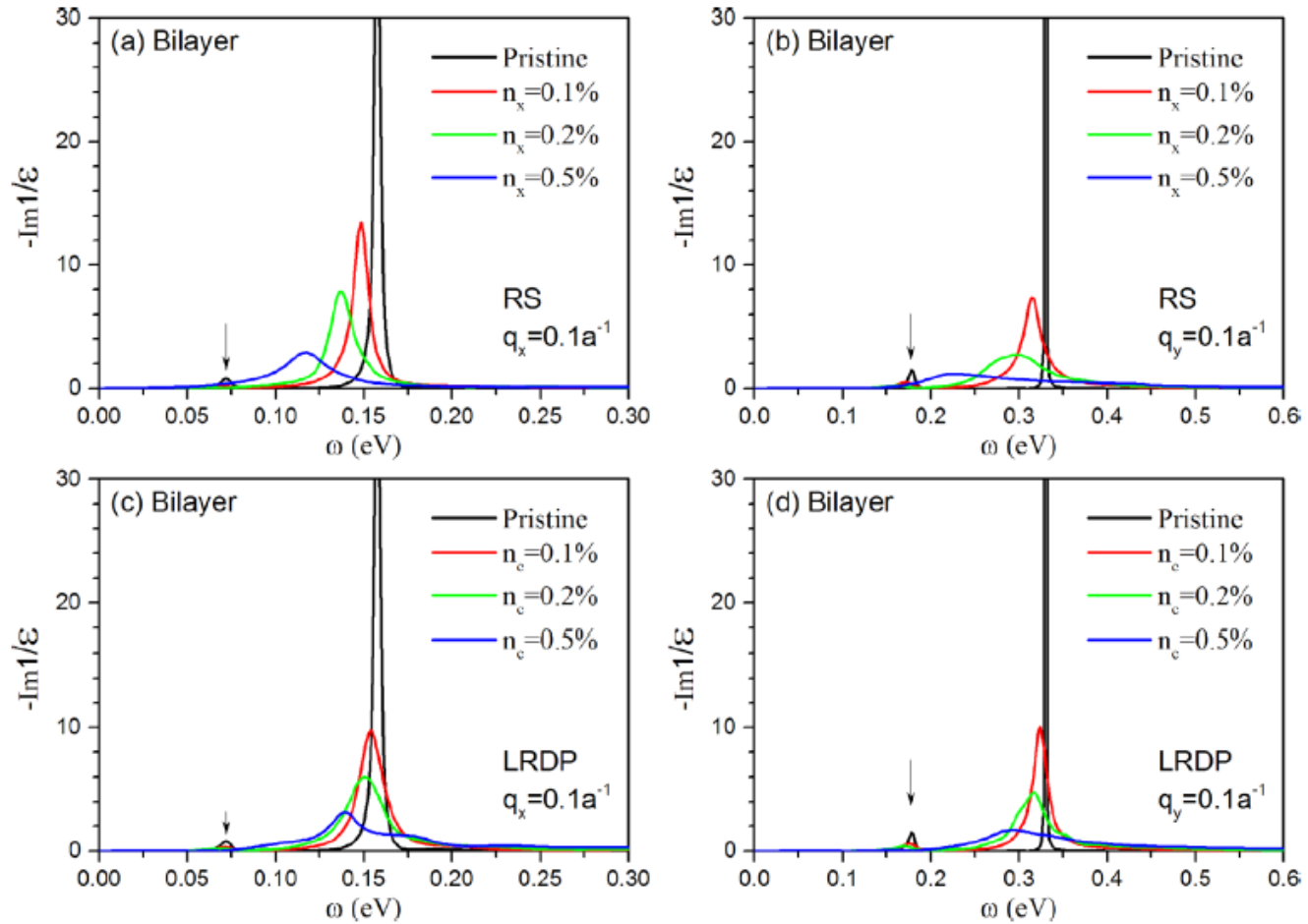


FIG. 7. (Color online) Energy loss functions of bilayer BP along zigzag (left) and armchair (right) directions. Panels (a) and (b) compare the loss function of pristine bilayer BP with that of samples with different concentrations of point defects. Panels (c) and (d) correspond to LRDP. All the results are calculated at $T = 300$ K. The peak marked by arrows in each panel correspond to the out-of-phase $\omega_-(q) \sim q$ plasmon (see text).

Plasmons: Biased Bilayer

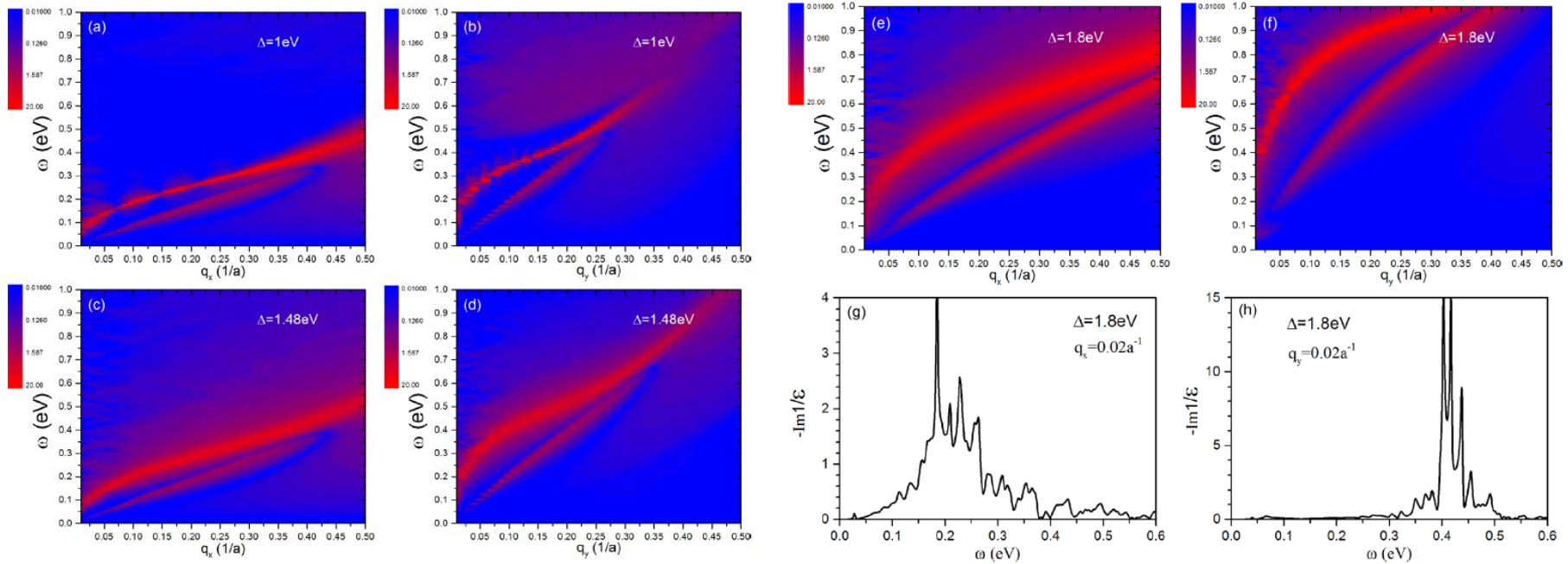


FIG. 9. (Color online) Energy loss functions of biased bilayer BP along zigzag (left) and armchair (right) directions. The strength of the biased potential is given in each panel.

Plasmon velocity is sensitive to bias (may tune plasmons by electric field!)

Plasmons have larger spectral weight in semimetal phase

Strong anisotropy of plasmon spectrum, essential difference between zigzag and armchair directions

Plasmons: Matrix formulation (local field effects)

D.A. Prishchenko, V.G. Mazurenko, MIK, and A.N. Rudenko, 2D Mater. 4, 027064 (2017)

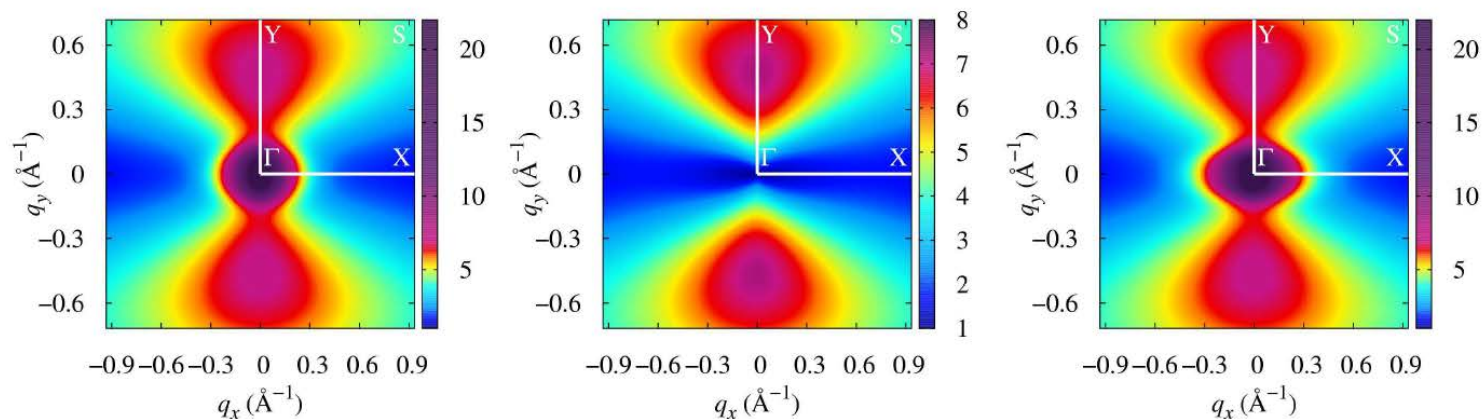


FIG. 4. Macroscopic static dielectric function $\epsilon_M(q_x, q_y)$ calculated for electron-doped (left), undoped (middle) and hole-doped (right) 1L-BP. Each plot shows distribution of ϵ_M over the whole BZ. Doping in both electron- and hole-doped cases corresponds to $n = 10^{13} \text{ cm}^{-2}$.

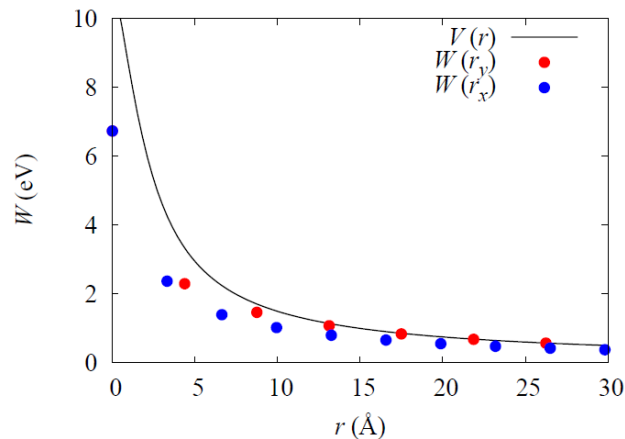


FIG. 5. Diagonal element of the screened Coulomb interaction matrix W calculated in real space along x - (blue) and y - (red) directions of 1L-BP. Unscreened (bare) interaction $V(r)$ is shown for comparison.

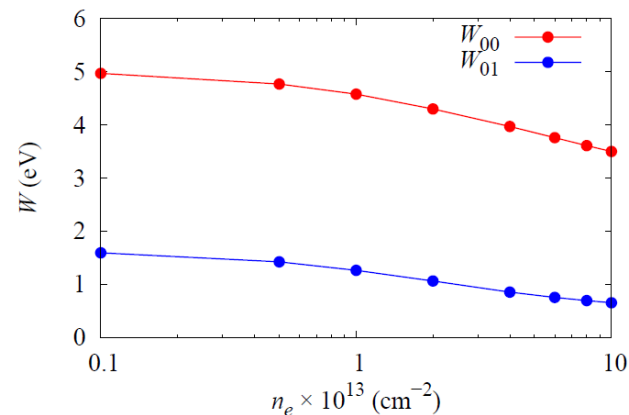


FIG. 6. On-site (W_{00}) and nearest-neighbor (W_{01}) screened Coulomb interaction in 1L-BP shown as a function of electron doping n_e . Red and blue lines are guide for the eye.

Plasmons: Matrix formulation II

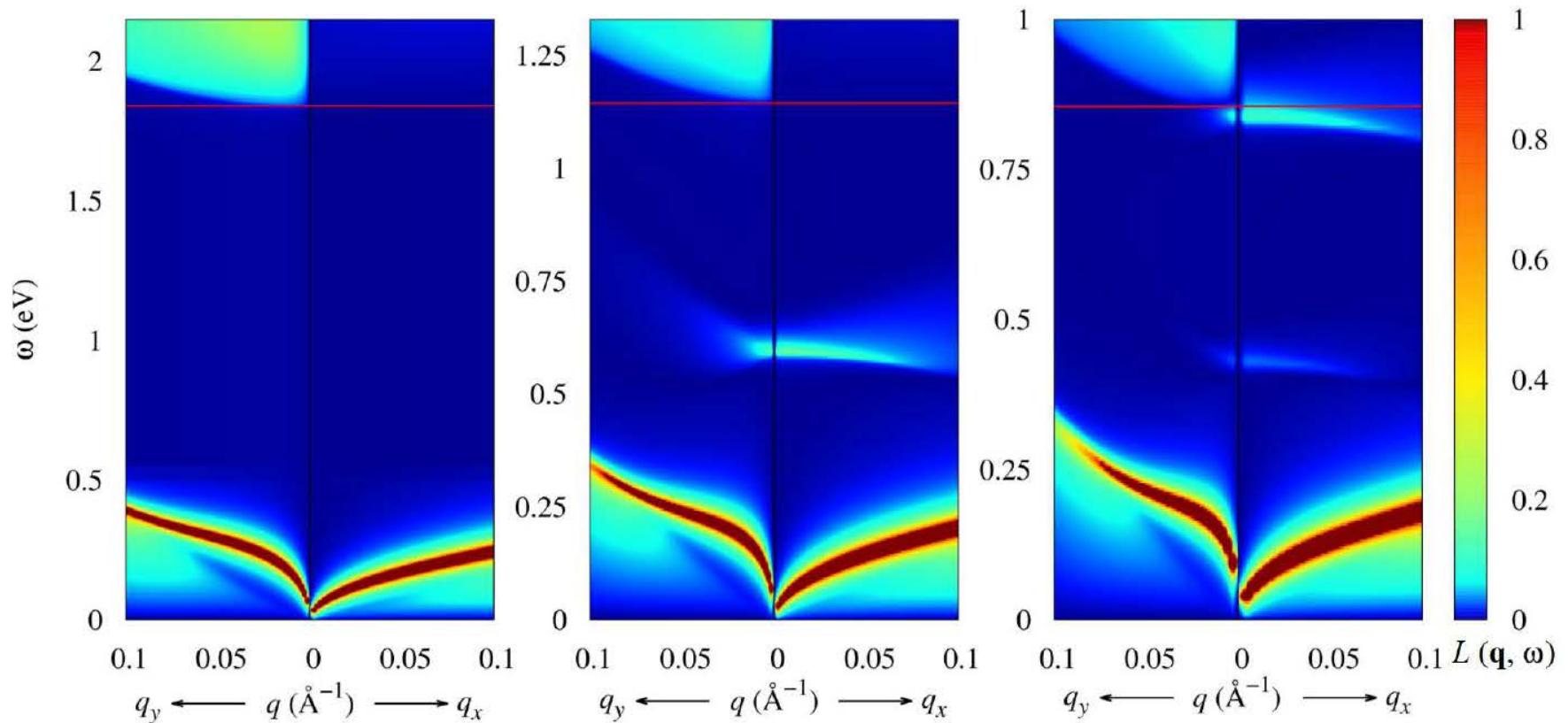
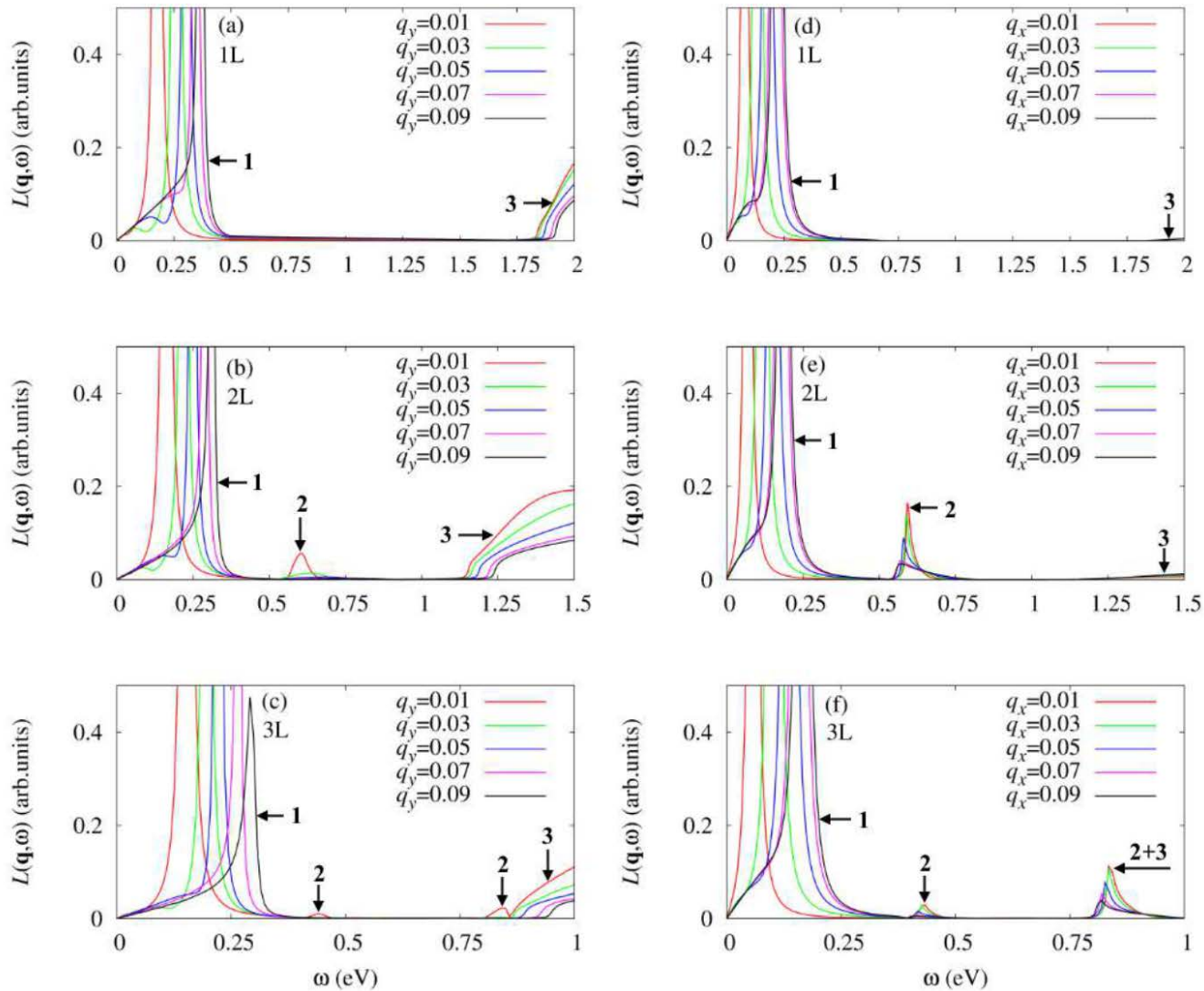


FIG. 7. Wave vector and frequency resolved loss function $L(\mathbf{q}, \omega)$ (shown in color) calculated for 1L-, 2L-, and 3L-BP. Left and right part of each spectrum corresponds to y - and x - direction, respectively. Red horizontal line marks an energy gap for each system. Note different scales along vertical (ω) axis. In all cases, electron-doping was used, corresponding to $n_e = 10^{13} \text{ cm}^{-2}$.

Plasmons: Matrix formulation III



EELS function for 1, 2, 3 layers of phosphorus: several plasmon branches are seen

Intrinsic mobility in single-layer BP

In graphene, two-phonon processes involving flexural phonons are more important than single-phonon processes involving in-plane phonons (except very low temperatures)

PRL 105, 266601 (2010)

PHYSICAL REVIEW LETTERS

week ending
31 DECEMBER 2010

Limits on Charge Carrier Mobility in Suspended Graphene due to Flexural Phonons

Eduardo V. Castro,¹ H. Ochoa,¹ M. I. Katsnelson,² R. V. Gorbachev,³ D. C. Elias,³ K. S. Novoselov,³
A. K. Geim,³ and F. Guinea¹

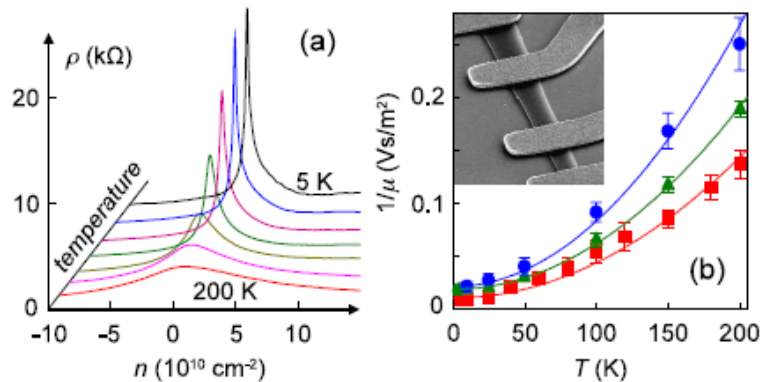


FIG. 3 (color online). (a) Electron transport in suspended graphene. Graphene resistivity $\rho = R(w/l)$ as a function of gate-induced concentration n for $T = 5, 10, 25, 50, 100, 150,$ and 200 K . (b) Examples of $\mu(T)$. The T range was limited by broadening of the peak beyond the accessible range of n . The inset shows a scanning electron micrograph of one of our suspended devices. The darker nearly vertical stripe is graphene suspended below Au contacts. The scale is given by graphene width of about $1 \mu\text{m}$ for this particular device.

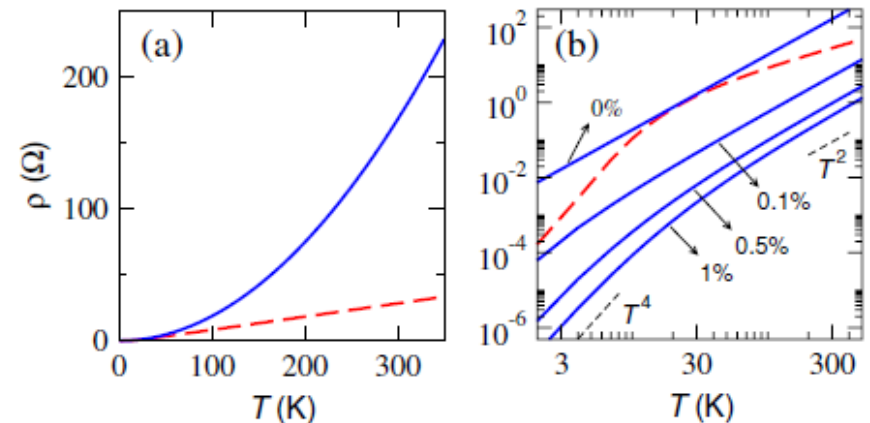


FIG. 2 (color online). (a) Contribution to the resistivity from flexural phonons (blue full line) and from in-plane phonons (red dashed line). (b) Resistivity for different strain. The in-plane contribution (broken red line) shows a crossover from a low to a high- T regime. In both cases, the electronic concentration is $n = 10^{12} \text{ cm}^{-2}$.

Intrinsic mobility in single-layer BP II

A. N. Rudenko, S. Brener, MIK, PRL 116, 246401 (2016)

What about black phosphorus?

Kubo-Nakano-Mori formula (corresponds to variational solution of Boltzmann equation)

Phonon energies at $q = 2k_F$ are supposed to be much smaller than $k_B T$ (the most relevant case)

$$\sigma_{xx} = \frac{e^2}{2S} \sum_{\mathbf{k}} \tau_{xx} v_{\mathbf{k}}^{x2} \left(-\frac{\partial f}{\partial \varepsilon_{\mathbf{k}}} \right) \quad \frac{1}{\tau_{xx}} = \frac{1}{\langle j_x^2 \rangle_e} \int_0^\infty dt \langle F_x(t) F_x^\dagger \rangle \quad \begin{aligned} F_x &= [j_x, H'] \\ H' &= \sum_{\mathbf{k}\mathbf{k}'} V_{\mathbf{k}\mathbf{k}'}^{\text{eff}} c_{\mathbf{k}}^\dagger c_{\mathbf{k}'} \end{aligned}$$

$$F_x = e \sum_{\mathbf{k}\mathbf{k}'} (v_{\mathbf{k}}^x - v_{\mathbf{k}'}^x) V_{\mathbf{k}\mathbf{k}'}^{\text{eff}} c_{\mathbf{k}}^\dagger c_{\mathbf{k}'} \quad \frac{1}{\tau_{xx}} = \frac{\pi}{\hbar} \frac{\sum_{\mathbf{k}\mathbf{k}'} \delta(\varepsilon_{\mathbf{k}} - \varepsilon_{\mathbf{k}'}) \left(-\frac{\partial f}{\partial \varepsilon_{\mathbf{k}}} \right) (v_{\mathbf{k}}^x - v_{\mathbf{k}'}^x)^2 \langle |V_{\mathbf{k}\mathbf{k}'}^{\text{eff}}|^2 \rangle}{\sum_{\mathbf{k}} v_{\mathbf{k}}^{x2} \left(-\frac{\partial f}{\partial \varepsilon_{\mathbf{k}}} \right)}$$

$\mathbf{k} = \mathbf{k}' + \mathbf{q}$

Parameters of interactions with in-plane and out-of-plane phonons are calculated from first principles

Intrinsic mobility in single-layer BP III

Single-phonon processes

$$\bar{E} = \frac{1}{2} \int d^2\mathbf{r} [C_{11}u_{xx}^2 + C_{22}u_{yy}^2 + 2C_{12}u_{xx}u_{yy} + 4C_{66}u_{xy}^2] \quad \text{Elastic energy}$$

$$\bar{V}_{\mathbf{q}}^{\text{eff}} = \bar{g}_{\alpha} u_{q_{\alpha}} q_{\alpha} \quad \text{Deformation potential of interactions with acoustic phonons}$$

$$\langle |\bar{V}_{\mathbf{q}}^{\text{eff}}|^2 \rangle = k_B T \frac{C_{66}(\bar{g}_x^2 q_x^4 + \bar{g}_y^2 q_y^4 - 2\bar{g}_x \bar{g}_y q_x^2 q_y^2) + (C_{22} \bar{g}_x^2 + C_{11} \bar{g}_y^2 - 2C_{12} \bar{g}_x \bar{g}_y) q_x^2 q_y^2}{C_{66}(C_{11} q_x^4 + C_{22} q_y^4 - 2C_{12} q_x^2 q_y^2) + (C_{11} C_{22} - C_{12}^2) q_x^2 q_y^2}$$

Intrinsic mobility in single-layer BP IV

Double-phonon processes

$$\tilde{E} = \frac{1}{2} \int d^2\mathbf{r} \left[\kappa_x \left(\frac{\partial^2 h}{\partial x^2} \right)^2 + \kappa_y \left(\frac{\partial^2 h}{\partial y^2} \right)^2 + 2\kappa_{xy} \frac{\partial^2 h}{\partial x^2} \frac{\partial^2 h}{\partial y^2} \right] \quad \text{Elastic energy}$$

$$\tilde{V}_{\mathbf{q}}^{\text{eff}} = \tilde{g}_{\alpha\beta} f_{\alpha\beta}(\mathbf{q}) \quad \text{Deformation potential of interactions with acoustic flexural phonons}$$

$$f_{\alpha\beta}(\mathbf{r}) = \frac{\partial h(\mathbf{r})}{\partial x_\alpha} \frac{\partial h(\mathbf{r})}{\partial x_\beta}$$

$$\begin{aligned} \langle |\tilde{V}_{\mathbf{q}}^{\text{eff}}|^2 \rangle &= \sum_{\mathbf{k}_1} [\tilde{g}_x k_{1x} (q_x - k_{1x}) + \tilde{g}_y k_{1y} (q_y - k_{1y})]^2 \\ &\times \langle h_{\mathbf{k}_1} h_{-\mathbf{k}_1} \rangle \langle h_{\mathbf{k}_1 - \mathbf{q}} h_{\mathbf{q} - \mathbf{k}_1} \rangle. \end{aligned} \quad (10)$$

For simplicity:

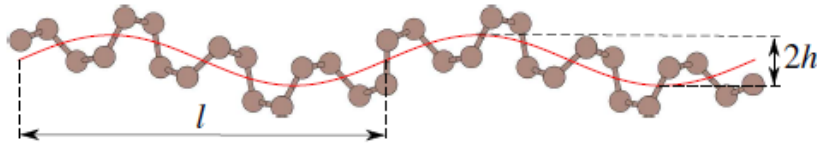
$$\kappa_{xy} = \sqrt{\kappa_x \kappa_y} \quad \langle h_{\mathbf{q}} h_{-\mathbf{q}} \rangle = \frac{k_B T}{(\sqrt{\kappa_x} q_x^2 + \sqrt{\kappa_y} q_y^2)^2}$$

Logarithmic cutoff of small q is required (like in graphene)

Intrinsic mobility in single-layer BP V

Ab initio calculations

(a) P armchair



(b) P zigzag

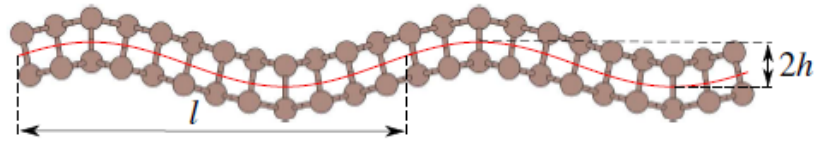
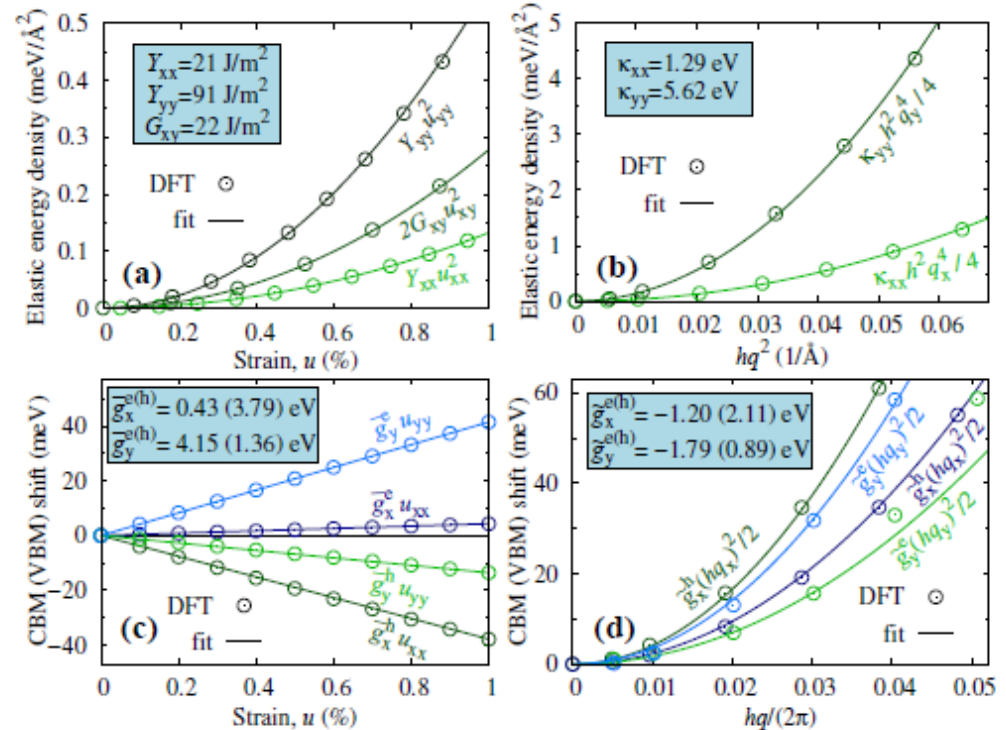


FIG. 1. (Color online) (a,b) Elastic energy and (c,d) band edge shifts as functions of in-plane and out-of-plane deformations in monolayer BP used to determine the elastic constants and deformation potentials involved in the calculation of carrier mobility. CBM and VBM stand for the conduction band minimum and valence band maximum, respectively. Points correspond to DFT calculations, whereas lines are the result of fitting with the constants shown in the insets. In-plane deformations are induced by direction-dependent strain (u), whereas out-of-plane deformations are characterized by the wave vector q and amplitude h of a sinusoidal corrugation along the armchair (x) and zigzag (y) directions [32].

Extracting deformation potentials from band shifts



Intrinsic mobility in single-layer BP VI

Energy dependence of effective masses are important (non-parabolic bands)

$$\varepsilon_{\mathbf{k}} = \frac{\hbar^2 k_x^2}{2m_x^E(\varepsilon)} + \frac{\hbar^2 k_y^2}{2m_y^E(\varepsilon)}$$

$$v_{\mathbf{k}}^{x(y)} = \frac{\hbar k_x(y)}{m_{x(y)}^V(\varepsilon)}$$

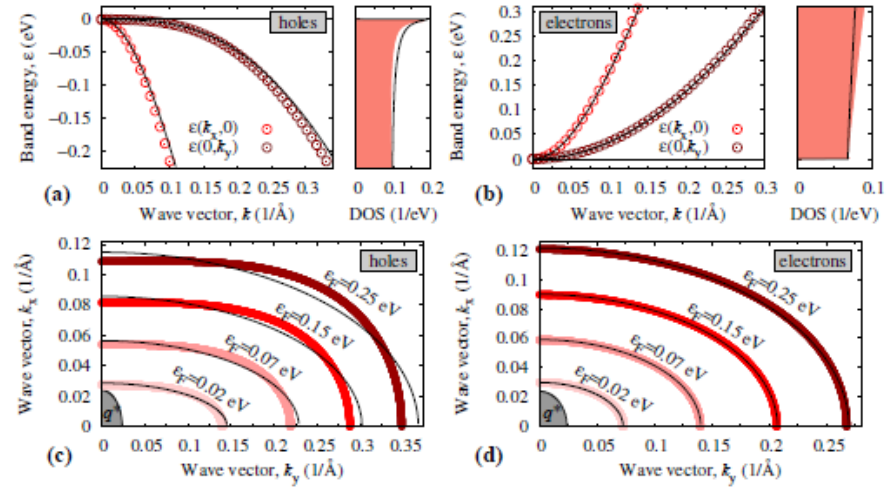
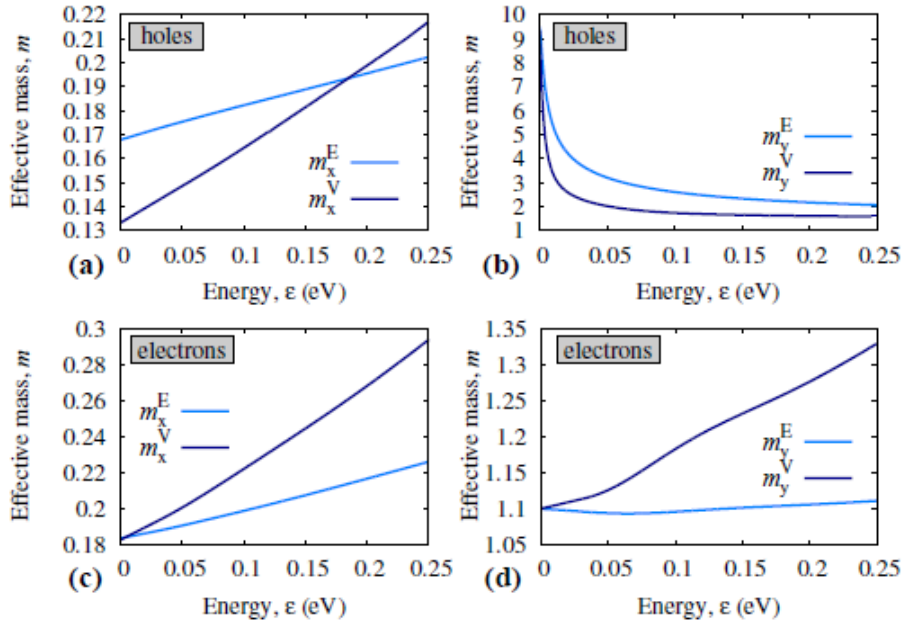


FIG. 5. (Color online) Energy dependence of the effective masses used in this work to approximate anisotropic dispersion (m_x^E , m_y^E) and band velocities (m_x^V , m_y^V) related to holes and electrons in monolayer BP.

FIG. 2. (Color online) (a,b) Energy dispersion of electrons and holes in monolayer BP along the armchair (x) and zigzag (y) directions with the related densities of states (DOS). (c,d) Fermi contours $\varepsilon_F = \varepsilon(k_x, k_y)$ shown for the irreducible wedge of the Brillouin zone. Points and thick lines are the result of GW_0 calculations [32], whereas thin black lines correspond to the model used in this work. Gray area marks the phonon cutoff wave vector q^* at $T = 300\text{K}$ (see text for details).

Intrinsic mobility in single-layer BP VII

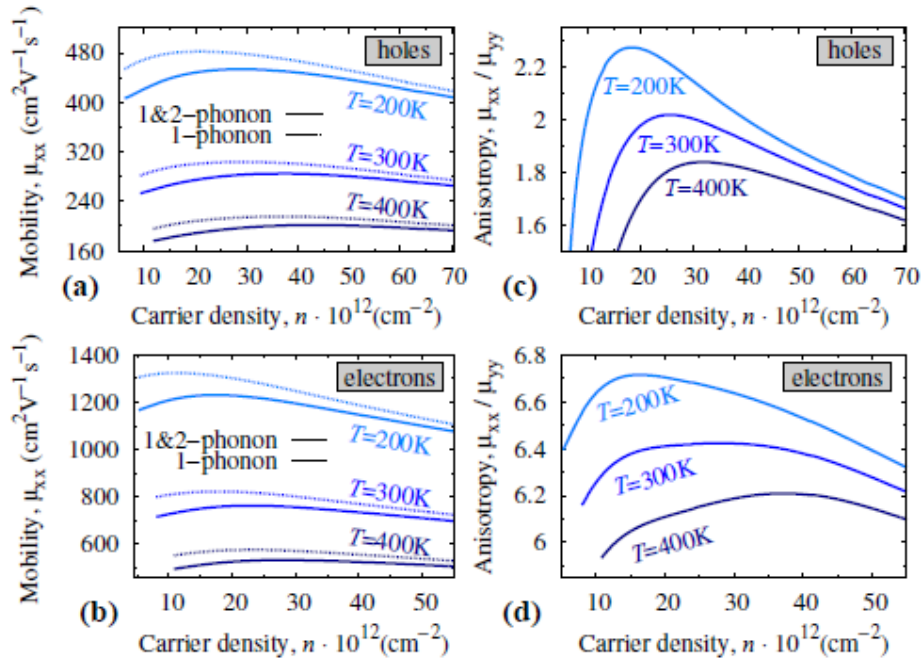


FIG. 3. (Color online) (a,b) Intrinsic carrier mobility (μ_{xx}) of monolayer BP shown as a function of the carrier concentration (n) calculated along the armchair direction for different temperatures (T). (c,d) Anisotropy of the carrier mobility represented at a ratio between the mobilities along the armchair and zigzag direction (μ_{xx}/μ_{yy}) shown for different T . Solid lines correspond to the contribution of both single-phonon and two-phonon scattering processes, whereas dashes lines to the single-phonon processes only. The lowest depicted density corresponds to the regime with $\ln(\bar{k}/q^*) > 1$.

Conclusions:

- (1) Contrary to graphene, single-phonon processes are more important @RT;
- (2) Intrinsic limit of mobility @RT 250 (700) cm²V⁻¹s⁻¹ for holes (electrons)

contrary to 10,000 for graphene;

- (3) Anisotropy of mobility is much stronger for holes than for electrons

(2),(3) seem to be in qualitative agreement with experiments on a few-layer phosphorus

Flexuron tail of density of states

PHYSICAL REVIEW B **82**, 205433 (2010)

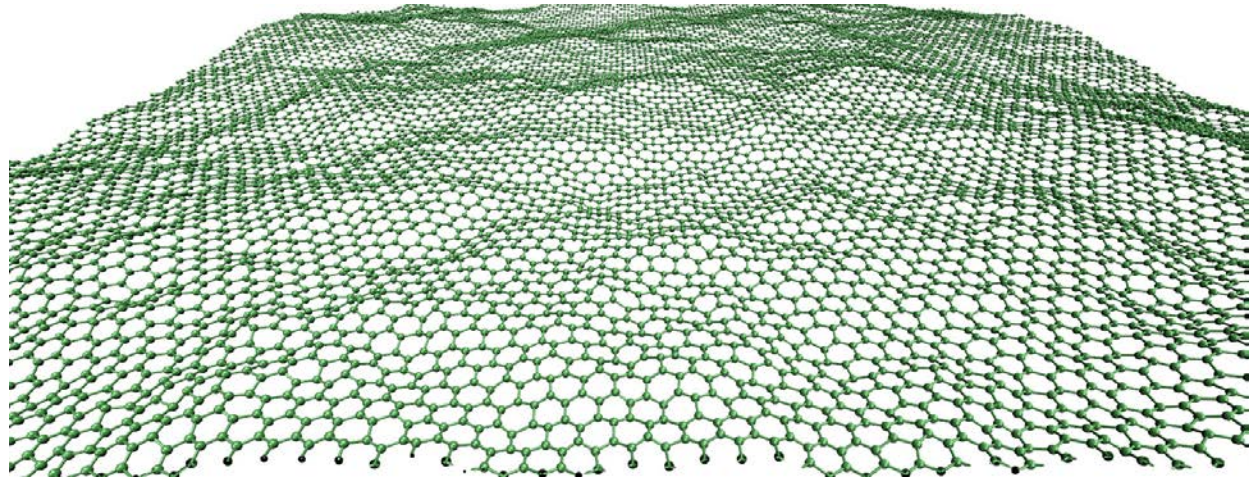


Flexuron: A self-trapped state of electron in crystalline membranes

M. I. Katsnelson

At finite temperature,
membranes are rippled

Snapshot: graphene @RT



Interaction with intrinsic ripples – the same as
two-phonon processes

Average position of band edge is shifted and fluctuation
tail appears (flexuron states)



Flexuron tail of density of states II

PHYSICAL REVIEW B **95**, 041406(R) (2017)

Effect of flexural phonons on the hole states in single-layer black phosphorus

S. Brener, A. N. Rudenko,^{*} and M. I. Katsnelson

Electron self-energy $\Sigma(E, \mathbf{p}) = \int \frac{d^2\mathbf{q}}{(2\pi)^2} \gamma(\mathbf{p} - \mathbf{q}, \mathbf{p}, \mathbf{q}, E) K_2(\mathbf{q}) G(E, \mathbf{p} - \mathbf{q})$

Without vertex corrections: self-consistent Born approximation. To take into account fluctuation tail (idea of L.V. Keldysh)

$$\gamma(\mathbf{p}, \mathbf{p}, \mathbf{0}, E) = 1 - \frac{\partial \Sigma}{\partial E} \quad \text{Ward identity} \quad \Sigma(E) = \left(1 - \frac{\partial \Sigma}{\partial E} \right) \int \frac{d^2\mathbf{q}}{(2\pi)^2} \frac{K_2(\mathbf{q})}{E - \epsilon_{\mathbf{q}} - \Sigma(E)}$$

Applied to holes in phosphorene, parameters from ab initio calculations:

$$\epsilon_{\mathbf{q}} = 2.9q_x^2 + 0.05q_y^2 + 13.2q_y^4 \quad (\text{atomic units})$$

Very anisotropic spectrum!

Flexuron tail of density of states III

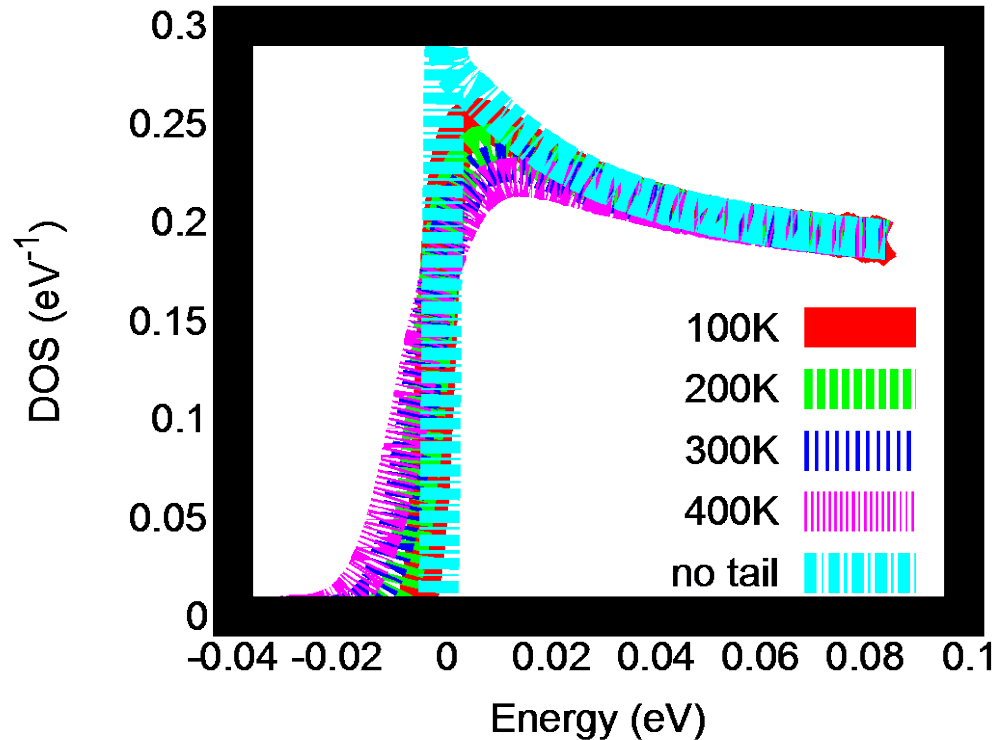


FIG. 1. DOS per unit cell per spin for $T = 100, 200, 300$ and 400 K. For reference, the DOS corresponding to bare dispersion without the inclusion of the flexuron tail is shown. The Van Hove singularity in the latter manifests the aforementioned quasi-one-dimensionality of the holes in black phosphorus. It is to a large extent smeared by the flexural modes.

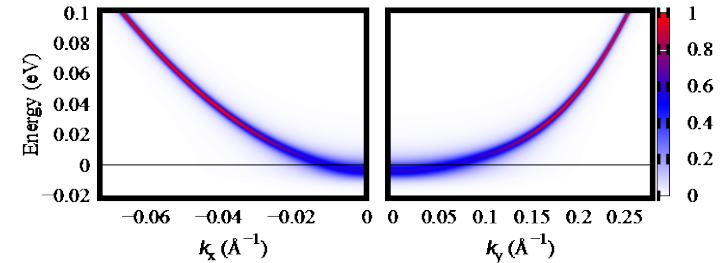


FIG. 2. Spectral function along k_x and k_y axis for $T = 300$ K. Note the different scale for the two plots.

Smearing of Van Hove singularity near the band edge by interaction with intrinsic ripples

Resume

- (1) Completely different physics from both graphene and transition-metal dichalcogenides
- (2) Strong difference of electronic structure from monolayer to bulk despite small cohesive energy
- (3) Insulator-semimetal transition under bias/potassium doping with anisotropic Dirac cones in bilayer black phosphorus
- (4) Very interesting defects, especially Co adatoms (single-atom orbital memory?!)
- (5) Tunable plasmonics?!
- (6) Mechanisms of intrinsic mobility quite different from graphene, much stronger interaction with acoustic phonons, strong limits on mobility

MANY THANKS
FOR YOUR ATTENTION